Nanoscale Advances

ROYAL SOCIETY OF CHEMISTRY

PAPER

View Article Online
View Journal | View Issue

Cite this: *Nanoscale Adv.*, 2025, **7**, 7620

From peels and coffee grounds to tunable carbon nanodots: waste-derived biocarbon meets ultrafast laser ablation

Karyme Nava,[a] Kamila González,[b] Víctor Castrejón,[c] Enrique Vigueras,[d] Jorge Reyes,[e] Miguel Camacho,[f] Zhiming Wang,[gh] Chengjie Wang,[h] Arup Neogi *[h] and Delfino Reyes*[hi]

Water-soluble, photoluminescent carbon nanodots (CNDs) were produced in minutes by picosecond-laser ablation of biocarbons obtained from orange peel, avocado peel, and spent coffee grounds. Mild pyrolysis at 350 °C first transformed the wastes into ash-free biocarbon with distinct degrees of aromatic ordering. Subsequent irradiation with 1064 nm, 150 ps laser pulses in water generated stable brown colloids whose optical and structural characteristics could be traced back to the precursor composition. Avocado-derived dots were the most abundant and smallest (2.2 ± 0.3 nm), displaying amorphous structure and bright blue-green emission centred at 430 nm under 330 nm excitation. In contrast, orange- and coffee-derived dots were larger (5–40 nm), partially graphitic, and markedly less emissive. Thermogravimetric and Raman analyses linked the superior yield and fluorescence of the avocado system to its high lignin content and oxygen-rich surface, favoring efficient laser fragmentation and creating abundant emissive surface traps. Excitation-dependent PL arises from these functional groups rather than size-quantisation, as corroborated by FTIR, XPS, and multi-peak PL deconvolution. The entire process avoids harsh chemicals, produces intrinsically water-dispersible nanodots, and valorises low-value biomass, offering a scalable, environmentally benign alternative to conventional hydrothermal or acid-oxidative syntheses. This work provides both mechanistic insight and practical guidelines for tuning CND performance through intelligent waste selection, opening new avenues for sustainable bio-imaging, sensing, and optoelectronic applications. This work establishes a direct feedstock-to-function relationship and positions ultrafast laser processing as a versatile, green platform for tailoring CND performance through rational waste selection.

Received 8th June 2025
Accepted 25th September 2025

DOI: 10.1039/d5na00560d

rsc.li/nanoscale-advances

Introduction

The imperative to develop sustainable, low-impact nanomaterials has spurred intensive research into carbon-based alternatives that can be sourced from abundant biomass and manufactured with minimal waste. Carbon nanodots (CNDs) have emerged at the forefront of this effort because their sub-10 nm sp^2/sp^3 cores, enriched with surface heteroatoms and defects, endow them with bright, tunable photoluminescence (PL) that is ideal for bio-imaging, chemical sensing, and flexible optoelectronics.[1–3] Unlike size-governed carbon quantum dots, the optical response of CNDs is dominated by surface chemistry—functional groups, vacancies, and edge states—yielding excellent aqueous dispersibility and inherent biocompatibility.[4–7] Various synthesis techniques have been developed to produce CNDs, including chemical oxidation,[8] hydrothermal processing,[9,10] and laser ablation.[11–13] Among these methods, pulsed laser ablation in liquid media has emerged as a particularly promising approach due to its ability to generate highly uniform nanoparticles with controlled size,

[a]*Bachelor's Degree in Biotechnology, Faculty of Sciences, Autonomous University of the State of Mexico, Toluca, Mexico*
[b]*Master Student at Department of Molecular Biomedecine, Center for Research and Advances Studies (CINVESTAV), Mexico City, Mexico*
[c]*TecNM/Technological Institute of Higher Studies of Jocotitlán, Jocotitlán, Mexico*
[d]*Laboratory of Research and Development of Advanced Materials (LIDMA), Faculty of Chemistry, Autonomous University of the State of Mexico, Toluca, Mexico*
[e]*Physics Institute, National Autonomous University of Mexico, University City, Coyocan, Mexico City, Mexico*
[f]*Laboratory of Photomedicine, Biophotonics and Ultrashort Pulse Laser Spectroscopy, Faculty of Medicine, Autonomous University of the State of Mexico, 50180 Toluca de Lerdo, Mexico*
[g]*Institute of Fundamental and Frontier Sciences, University of Electronic Science and Technology of China, Chengdu, People's Republic of China*
[h]*Institute for Advanced Study, Chengdu University, Chengdu 610106, PR China. E-mail: dreyesc@uaemex.mx; arup@uestc.edu.cn*
[i]*Laboratory of Opto-Acoustics and Nanomaterials (LOAN), Faculty of Science, Autonomous University of the State of Mexico, Toluca, Mexico*

morphology, and optical properties.[14,15] This technique involves irradiating a carbon precursor, in the form of solid targets[16] or micro- and milli-powders,[17,18] neither immersed nor suspended in a liquid medium, with a focused high-energy pulsed laser. The laser-induced ablation and fragmentation of the carbon material result in the formation of CNDs with well-defined structural and optical characteristics, whose features depend on the laser parameters and solvent features.

The use of waste materials as precursors for the synthesis of CNDs has gained significant attention in recent years, driven by the dual objectives of waste valorisation and the development of sustainable nanomaterials. Agricultural and food processing waste, such as fruit peels and other biomass, has been demonstrated as an effective carbon source for CND synthesis.[19–21] The conversion of waste into CNDs involves utilizing non-edible parts of fruits and vegetables,[22,23] as well as more complex food waste as meals-industry wastes,[24,25] household green wastes,[26] oils,[27] and agro-industrial byproducts,[28] among others. Several studies have reported the successful production of CNDs from waste materials, particularly through hydrothermal synthesis. This thermally driven approach, which employs pressurized autoclave vessels at reaction temperatures typically ranging from 120 to 240 °C, has been used to process a wide variety of waste precursors, including pomelo, strawberries, tamarind, white onion, and several region-specific flowers.[29,30] Similarly, these routes have been employed to synthesize CNDs from grape peels,[31] wine corks,[32] and beer bagasse,[33] among others. A comprehensive list of waste-derived precursors can be found in ref. 29, 34, 35, demonstrating the versatility of using waste materials hydrothermally treated for CNDs production with different features, mainly suspended in water.

The pyrolysis of waste materials has also been explored to produce CNDs. This process typically requires temperatures ranging from 300 to 900 °C to facilitate CNDs formation. As a result of pyrolysis, biocarbon (biochar) is obtained, which is then processed to yield CNDs through pulverization, suspension in a solvent, sonication, centrifugation, and/or lyophilization. CNDs synthesized *via* pyrolysis have been derived from various waste sources, including olive solid waste, where the pyrolysis temperature was found to influence the quantum yield but not the maximum emission wavelength.[36] Other studies have reported the production of CNDs from sago industrial waste,[37] rice husk pyrolysis,[38] pyrolyzed black seed powders,[39] and biocarbon obtained from date palm waste.[40] Additionally, a combination of pyrolysis and ultrasonic treatment has been used to process rice straw,[41] and spent coffee grounds following chemical treatment, sonication, and laser fragmentation process.[42] The last study demonstrated the production of CNDs from carbonized spent coffee grounds, which were chemically treated with acetone, toluene, and other solvents. This approach yielded stable, luminescent colloidal suspensions following sonication and pulsed laser irradiation, highlighting the potential of pyrolysis-based methods for generating high-quality CNDs, but still requiring organic solvents to reach their final properties.

This paper highlights the potential of utilizing waste-derived biocarbon as precursors in combination with short-pulsed laser-based materials processing for the synthesis of water-soluble and photoluminescent carbon nanodots. Specifically, pulsed laser ablation in liquid media was employed to fabricate CNDs from biocarbon derived from organic waste materials, including orange peel (OP), avocado peel (AP), and spent coffee grounds (SCG). The biocarbon was produced in a high-energy furnace, and the results demonstrate that CNDs synthesized from these sources exhibit distinct structural and optical properties, emphasizing the critical role of precursor composition in determining nanomaterial characteristics. Furthermore, this study underscores the importance of understanding the structural features of waste-derived biocarbon, as they directly influence the size, crystallinity, and photoluminescence behaviour of the resulting CNDs. Integrating pulsed laser ablation with biocarbon precursors provides a promising route to produce water-soluble CNDs, which could be directly applied in bio-experiments as bioimaging and sensing.

Experimental

Materials and methods of characterization

Biomass's thermal degradation analysis. The thermal degradation of three biomass materials, orange peel (OP), avocado peel (AP), and spent coffee grounds (SCG), was analyzed using calorimetric techniques. In the initial step, the biomass was dried at 70 °C in an oven for 120 minutes, followed by fragmentation in a mortar until the particle size was reduced to less than 1 mm. The degradation process was studied using Thermogravimetric Analysis (TGA), conducted with a Sensible Thermal Analyzer STA 8000 (PerkinElmer) coupled with Differential Scanning Calorimetry (DSC). For each biomass, approximately 25 mg was placed in the sample holder. The heating process began at room temperature (25 °C) and increased to 800 °C at a rate of 20 °C per minute. Nitrogen was used as purge gas to maintain a non-oxygen environment during the experiments. Due to the absence of oxygen, the residues produced from the TGA calorimeter can be considered pyrolyzed biocarbon. The carbonized materials, recovered from the calorimeter, were stored for subsequent structural characterization.

Structural characterization of the TGA-biocarbon. The carbonized biomasses (biocarbon – BC-) recovered from the TGA calorimeter container were structurally characterized using Raman spectroscopy and Scanning Electron Microscopy (SEM). Raman analysis of the three biocarbon samples was performed with a Raman spectrometer (Horiba Jobin Yvon XploraPlus). A 785 nm wavelength laser was used as the excitation source, with a nominal power of 50% of 100 mJ. A 50X objective lens focused the laser beam onto the samples, while scattered light was collected and directed to a coupled charge-coupled device (CCD) camera. The Raman spectra for each sample were acquired with an integration time of 2 s using a 1200 lines per mm grating. The spectra spanned a wavenumber range from 1000 to 3750 cm^{-1}.

Surface morphology features of each BC were obtained through SEM micrographs using an electronic microscope (Jeol)

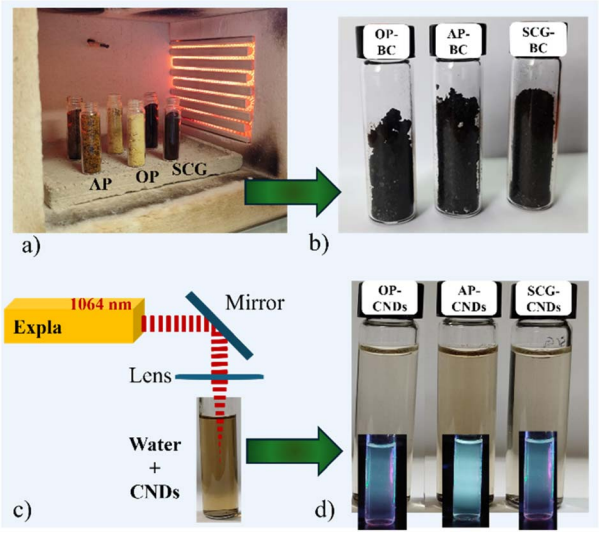

Fig. 1 Steps to produce CNDs from laser ablated waste derived-biocarbon. (a) Wastes before the thermal degradation in the high-energy furnace, (b) obtained biocarbon, (c) pulsed laser ablation process of the biocarbon, and (d) CNDs systems from each biocarbon.

model JSM-IT100. The microscope was operated in high vacuum mode with an acceleration voltage of 12 kV. For surface elemental composition analysis, SEM analysis was complemented by Energy Dispersive Spectroscopy (EDS), with an acceleration voltage of 20 kV.

Production of biocarbon in a high-temperature furnace. Large-scale BC production was conducted in a high-temperature furnace (Evelsa), as described in Fig. 1a. The furnace was heated from room temperature to 350 °C at a temperature ramp of 20 °C min^{-1}. As previously described, the dried biomasses were placed in six borosilicate containers, with a total biomass weight of approximately 20 g. Once the furnace reached 350 °C, the biomass was introduced into the furnace and maintained at this temperature for 30 minutes. This temperature was selected to maximize biocarbon yield while preventing ash formation, which was optimized by several extra experiments at different temperatures. After the specified time, the three types of BC (Fig. 1b), OP-BC, AP-BC, and SCG-BC, were removed from the borosilicate containers, transferred to new containers, and pulverized to obtain biocarbon dust. The biocarbon samples were structurally characterized as described in the previous section for the TGA-recovered biocarbon, *i.e.*, using Raman and SEM techniques.

Synthesis of carbon nanodots by pulsed-laser method. The experimental setup used for synthesizing water-soluble carbon nanodots (CNDs) from biomass-derived biocarbon using the pulse-laser technique has been previously reported for other types of raw carbon.[18] In this study, the setup utilized an infrared pulsed laser (Expla) emitting at a wavelength of 1064 nm (sketched in Fig. 1c), with a pulse duration of 150 picoseconds and a constant average energy output of 30 mJ, and a repetition rate of 10 Hz. 0.1 g was placed at the bottom of a glass container for each BC type. The container was then filled with 6 mL of distilled water. Each BC was observed to be insoluble in water; it remained intact and sedimented at the bottom and on the water surface. The laser beam was focused using a lens with a focal length of 30 cm, with the focal point positioned approximately 1.5 cm above the base of the glass container, which had a total height of 5 cm, as illustrated in Fig. 1c. During the initial stage of the laser irradiation process, the laser pulses interact with the BC, initiating the laser ablation process, resulting in their fragmentation. The fragmented BC particles became suspended in the water, forming a colloidal dispersion, with a continuous re-fragmentation. Manual agitation was applied during this phase to enhance the breakup process.

Irradiation was performed for a total of 10 min, resulting in a brownish colloidal solution. Non-fragmented BC remained sedimented at the bottom of the container. The CBDs' colloidal suspension was then left undisturbed for two hours to allow further sedimentation of larger particles and unfragmented material. Subsequently, 5 mL of the colloidal solution was carefully extracted, ensuring that the sedimented material was not disturbed. The extracted colloidal suspension, containing the synthesized carbon nanodots, was used for optical and structural characterization. This procedure, under the same conditions, was conducted for the three types of BC to produce orange peels (OP-CNDs), avocado peels (AP-CNDs), and spent coffee grounds (SCG-CNDs)-carbon nanodots, as previously discussed. Images of the resulting colloidal CNDs for each biocarbon source are shown in Fig. 1d, which are actual pictures of the CNDs' colloidal suspensions after two hours from their synthesis, as described above.

Structural and morphological characterization of CNDs. A similar Raman analysis was performed in previous sections to gain insight into the structural features of the as-prepared CNDs. For this purpose, 10 drops of each CND solution were manually dropped on a glass slide and dried under lab conditions. This analysis was completed using FTIR analysis. It was performed as follows: FTIR spectra of the three dried biomasses, the biocarbon products in the high-energy furnace, and the corresponding CNDs produced from these three biomasses. This analysis provided insights into the transformation of biomasses until they reached the CNDs, as well as which components of each biomass were retained in the final products, thereby elucidating their structural and optical properties. The sample was prepared as required using a PerkinElmer FTIR spectrometer in the 400–4000 cm^{-1} wavenumber range.

The morphological features of the produced CNDs were examined *via* Transmission Electron Microscopy (TEM) in a JEM-2010F model operating at 200 KV. Samples were prepared by dropping three drops on a copper grid. HRTEM was used to gain insights into the atomic layer features.

CND's optical characterization. The optical properties of the three CND colloidal systems were analyzed using UV-Vis spectroscopy within the wavelength range of 300 to 700 nm, employing a single-beam spectrometer (VELAB). A quartz cuvette with a 1 cm path length was used as the sample holder and filled with 3.5 mL of the CND solutions. The primary optical

characteristic of interest was the photoluminescent response of the CNDs colloids, as this property indicates whether the raw biomass source for the biocarbon influences their optical behavior. To evaluate photoluminescence, a spectrofluorometer (Fluoromax-P) was used to measure the emission of light upon excitation at various wavelengths ranging from 330 to 490 nm, in increments of 20 nm. As will be demonstrated below, not all excitation wavelengths stimulated a measurable light emission, highlighting the selective excitation-dependent photoluminescent behavior of the synthesized CNDs.

Time-resolved photoluminescence spectroscopy. The carbon quantum dots' time-resolved spectroscopy was measured using the Harpia-TF time-resolved fluorescence spectrometer (light conversion), which combines time-correlated single photon counting (TCSPC) techniques. The samples were excited at 350 nm, respectively, and the emission spectra were collected at different emission wavelengths, from 410 nm to 550 nm. Some of them were analyzed for comparison.

Results and discussion

Calorimetry

Results on the biomass thermal degradation. As described, the thermal degradation of the biomasses, OP, AP, and SCG, was studied using TGA and DSC analysis. Fig. 2 illustrates the TGA (dashed black lines) and DTG (coloured lines) results for the thermally analysed biomasses. TGA thermograms facilitated the identification of distinct weight percentage loss stages at specific temperatures. Fig. 2a corresponds to the thermogram of the OP biomass (blue line), 2b for the AP biomass (purple line), and 2c for the SCG biomass (orange line), from which minimal mass loss percentages were observed between 30–150 °C, namely 5.81%, 5.72%, and 7.08%, respectively. These primary weight-losses are attributed to the evaporation of water content and the volatilization of certain light compounds.[43] The corresponding DTG peaks were observed between 75–82 °C for the three samples.

For the OP biomass, the thermogram revealed three distinct mass loss stages due to the thermal degradation of its components. The initial mass loss of 32.24%, occurring between 150–285 °C, corresponding to the DTG peak at 223 °C, is associated with pectin degradation. The second stage, identified by the DTG peak between 285–375 °C (centred at 346 °C), accounts for 23.93% of mass loss and results from the degradation of hemicellulose and cellulose. The third stage, representing a 12.95% mass loss, occurs between 375–580 °C and is attributed to the degradation of lignin and homologous phenolic compounds. Previous studies have reported pectin and hemicellulose degradation at 250 °C, while cellulose and lignin degradation occur at 340 °C and 487 °C, respectively.[44] In the

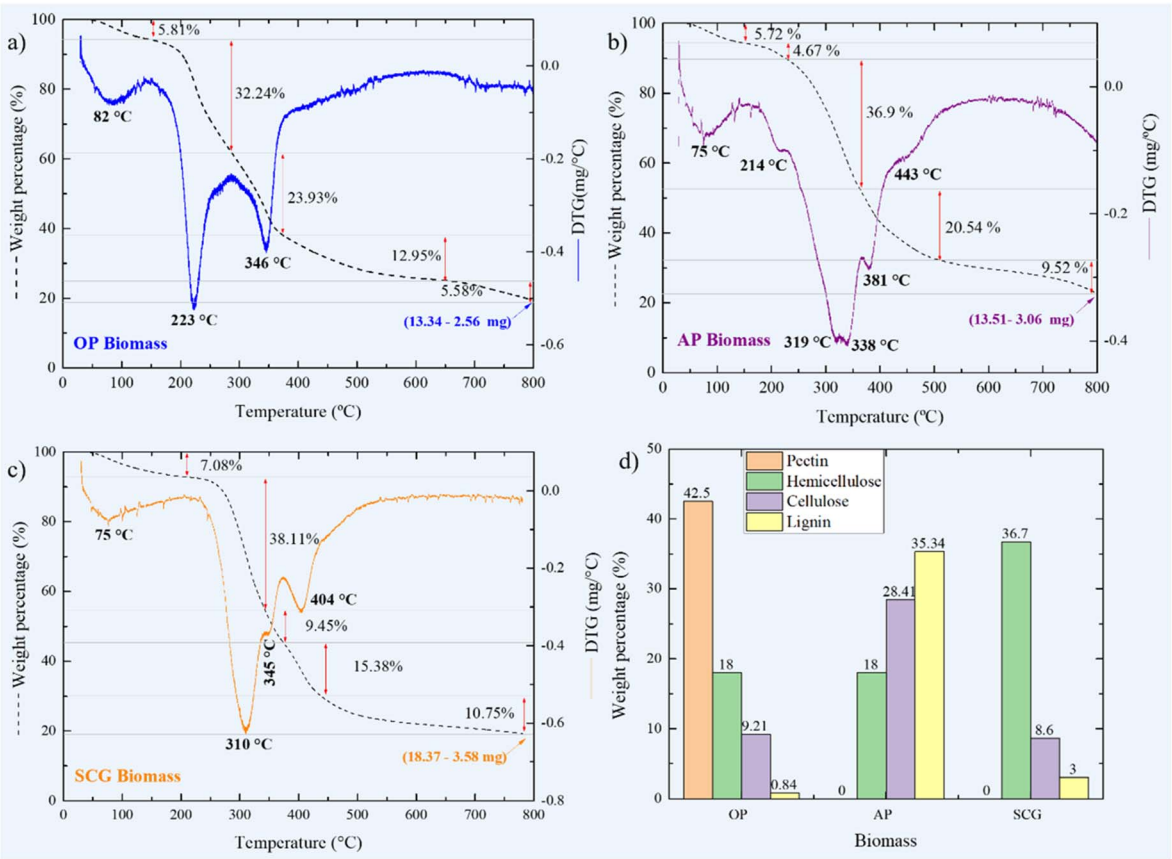

Fig. 2 TGA and DTG analysis for the thermal degradation of the organic wastes. TGA and DTG thermograms for the (a)-OP sample, (b)-AP sample, and (c)-SCG sample; (d) contains the weight percentage of each main component of the analysed organic wastes.

temperature range of 580–800 °C, the observed 5.58% mass loss is associated with the complete carbonization of the sample. It is convenient to report on the TGA experiment. 13.34 mg of orange peel was used, yielding 2.56 mg, which corresponds to a biocarbon production of 19.19% of the raw material. This transformation was conducted within a controlled environment (calorimeter) at a maximum temperature of 800 °C.

Similar mass loss stages were recorded with different percentages of loss in the AP biomass. The most noticeable loss occurred between 250–400 °C, related also to hemicellulose and cellulose degradation, recorded as a 36.9% loss; the DTG peak at 443 °C can be attributed to lignin degradation, whose loss comprises 20.54%. It has been reported that the degradation of several gaseous compounds such as CO, CO_2, CH_4, CH_3COOH, and HCOOH for avocado peel occurs between 600–800 °C,[45,46] which is observed as 9.52% of mass loss in the thermogram and could also be present in the OP biomass. The biocarbon transformation allowed the production of 3.06 mg of biocarbon from a waste raw of 13.51 mg, meaning a yield of 22.64%. For the SCG biomass, it showed a large percentage of mass loss, 38.11%, between 200–350 °C, with two DGT peaks at 310 °C and 345 °C, and an extra one at 403.6 °C. These peaks correspond to the thermal degradation of the cellulose, hemicellulose, and fatty acids, respectively.[47,48] In this case, the yield was similar to that of the orange peel waste, at 19.48%, indicating the avocado peel was 3% higher than the other two waste samples. The mentioned yields will be compared with those when the biocarbon is produced in a high-energy furnace, which is important to scale up the production of the waste-derived biocarbon.

The thermal degradation of the three organic samples utilized in waste-derived biocarbon production occurs in three main stages: evaporation of moisture, active pyrolysis, and passive pyrolysis. Active pyrolysis, characterized by significant mass loss, is associated with the degradation of the principal components of lignocellulosic matter, namely, hemicellulose, cellulose, and lignin, and in the case of the orange peel, pectin. Cellulose undergoes pyrolysis within the temperature range of 315–390 °C, with continued degradation beyond 390 °C at a reduced mass loss rate, while the corresponding degradation of hemicellulose occurs between 220–315 °C.[49] In the case of lignin, it exhibits a gradual mass loss rate (<0.15%/°C) from room temperature to 700 °C, resulting in approximately 40% mass loss due to its slow carbonization to form biocarbon primarily; this detail, as will be shown below, conveniently promotes the formation of fragile biocarbon. The thermal degradation of lignin is a many-sided process comprising three stages. The initial stage, emerging between ambient temperature and 100 °C, involves moisture loss. The subsequent stage spans 200 °C to 400 °C, attributed to the cleavage of β–O–4 aryl ether bonds and the elimination of lignin side chains, leading to an approximately 40% mass loss.[50] Finally, a mass loss of about 10% occurs between 400 °C and 700 °C, attributed to the degradation of the primary aromatic rings. Consequently, this stage of mass loss can be construed as the simultaneous decomposition of several compounds.[51]

Fig. 2d is a comparative plot of the amount of the three main components of the under-analysis organic wastes. The OP biomass exhibits lower thermal stability, manifesting an earlier onset of mass loss compared to the other two samples. In contrast, the AP demonstrates the least mass loss when compared with the orange peel and the used coffee grounds. This difference can be attributed to the thermal degradation behaviour, intricately linked to the sample's composition. The OP primarily comprises pectin, hemicellulose, and cellulose, compounds with lower thermal stability across distinct temperature ranges. This susceptibility arises from their low molecular weight and structural linkage through glycosidic bonds and hydrogen bridges, leading to substantial weight loss during degradation. The components are well-thermally stable, and structural modification can be promoted. Conversely, the AP consists of hemicellulose, cellulose, and a higher proportion of lignin (35.34%). The aromatic groups were characterized within this composition, emerging as the most thermally stable compound, which has an impact on the molecular reorganization during thermal degradation. The pectin structure, interconnected through covalent and glycosidic bonds, necessitates higher temperatures for degradation, reaching up to 900 °C.[50] Consequently, the slow carbonization process results in a higher yield following the calcination process, as corroborated by thermogravimetric analysis. In the case of the SCG biomass, which possesses a higher proportion of hemicellulose and cellulose, it degrades within a comparable temperature range to that of orange peel due to shared structural characteristics. Notably, cellulose exhibits a greater molecular weight, coupled with a reduced proportion of lignin, imparting increased stability to mass loss after the degradation of its constituents.

Structural analysis

Raman results of the TGA-biocarbon. To elucidate the structure of the carbonized biomasses recovered from the TGA calorimeter, Raman spectroscopy was employed to obtain spectra characterizing each one, as illustrated in Fig. 3a–c for OP-BC, AP-BC, and SCG-BC biocarbon, respectively. As this Raman analysis was performed using the biocarbon obtained from the calorimeter used to make the TGA analysis, a maximum temperature of 800 °C with a controlled temperature ramp of 20 °C min^{-1} is the degradation condition. The principal Raman bands for carbonaceous materials are the D (1300–1400 cm^{-1}) and G (~1580 cm^{-1}) bands. The former signifies structures originating from disorder or the presence of defects, correlated with the vibration of the carbon system possessing more than six aromatic rings; this commonly arises from the pyrolysis of cellulose, xylenes, and lignin.[51–53] The latter is linked to carbon graphite, attributed to the E_{2g} vibration mode of the graphitic carbon structure with sp^2 bonds. Both Raman bands were observed within the mentioned wavenumber interval for the three samples; the D-band was recorded with slight variations at 1310 cm^{-1}, 1305 cm^{-1}, and 1312 cm^{-1}, for the OP-BC, AP-BC, and SCG-BC, respectively, while the G-band was correspondingly at 1564 cm^{-1}, 1572 cm^{-1}, and 1560 cm^{-1}, as can be seen in Fig. 3.

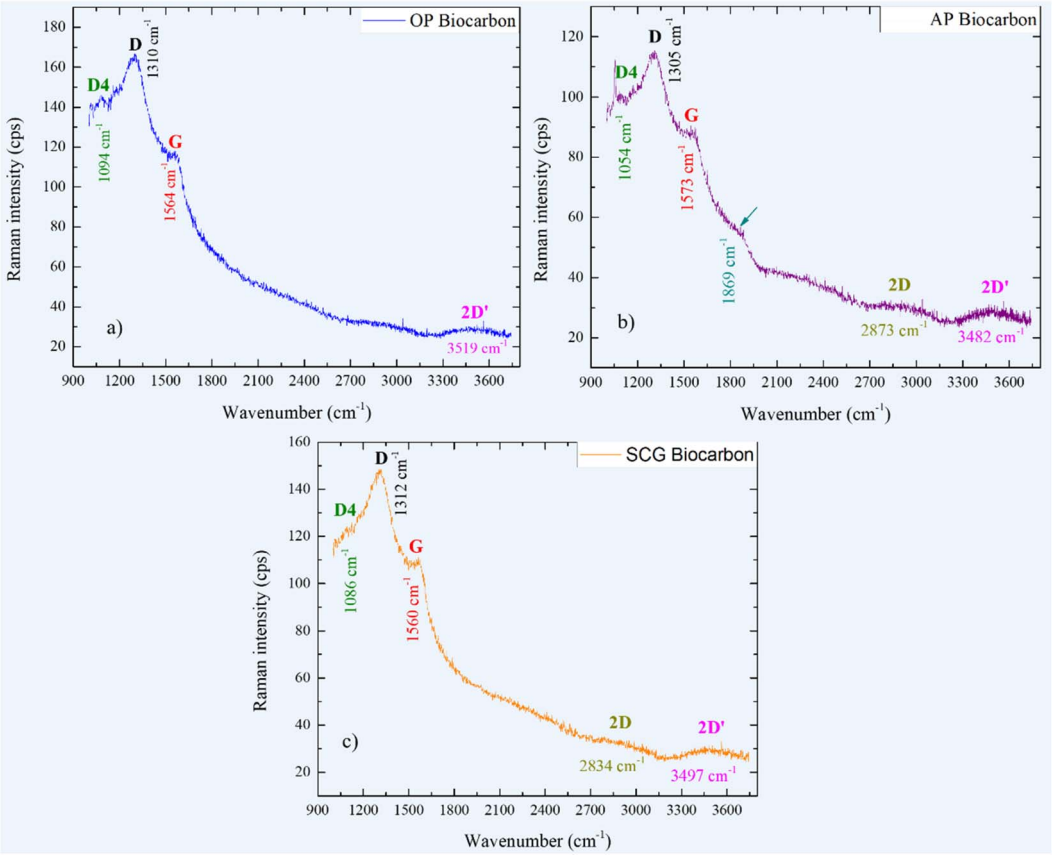

Fig. 3 Raman analysis of the biocarbon derived from the TGA equipment. (a) corresponds to the Raman spectra for the OP sample, being (b) for the AP sample, and (c) for the SCG sample, where the typical Raman bands for carbon-based materials have been identified.

The presence of a third Raman band in the three samples, referred to as D_4 or I-band, observed at 1172 cm^{-1}, 1054 cm^{-1}, and 1086 cm^{-1} for the OP-BC, AP-BC, and SCG-BC, is associated with disordered graphitic lattice (A_{1g} symmetry), polyenes, sp^2–sp^3 ionic impurities,[54–56] C=C or C–C stretching.[57] In the case of biocarbon derived from AP, an additional Raman mode at 1869 cm^{-1}, which is not common in carbonaceous materials, could be attributed to a L-band at 1835 cm^{-1} for single-walled carbon nanowires,[58] but a more exhaustive analysis is required to ascertain the origin of these extra Raman signals that were detected after 2500 cm^{-1} (Fig. 3), in all three samples, which are related to the presence of graphene sheets, as the 2D and 2D′ Raman bands were identified. The Raman results suggest the presence of a similar type of biocarbon in the three BC samples.

An important factor to consider in the Raman analysis of carbon-based materials is the relationship between the intensity of the D band and the G band, which indicates the degree of their structural disorder.[55] The ratio of the intensities I_D/I_G Raman peaks is 1.41 for the OP-derived biocarbon, 1.27 for the AP-BC, and 1.34 for the SCG-BC. As the I_D/I_G ratio increases, the density of defects in carbon materials increases, such as edge defects and vacancies, which occur in the case of amorphous graphite because it lacks a regular crystalline structure, an effect that can be derived from the increase in temperature.[54–56] It has been associated with the increase in the intensity of the D band with respect to the G band, which increases the pyrolysis temperature because of the formation of aromatic rings and carbon crystallites in the biocarbon.[59]

It is well-known that the Raman spectra can be analysed by fitting Lorentzian curves, which allows for in-depth identification of the specific peaks that compose them. The analysis of the OP-derived biocarbon is presented in Fig. 4a, which shows that the Lorentzian fit yields fitting peaks at 1085 cm^{-1}, 1300 cm^{-1}, and 1510 cm^{-1}, corresponding to the D_4 bands, D and G bands, respectively.[60] For the AP-BC, presented in Fig. 4b, four fitting peaks were found at 1058 cm^{-1}, 1322 cm^{-1}, 1542 cm^{-1}, and 1774 cm^{-1}, while the first three correspond to, as for the OP, the Raman bands D_4, D, and G, respectively; the fourth is assigned to the L Raman band, as has already been mentioned. Fig. 4c shows the analysis of the SCG-BC, in which the main peaks were determined through the fitting at 1079 cm^{-1}, 1318 cm^{-1}, and 1561 cm^{-1}, the latter being the peaks corresponding to bands D and G, while the peak present at 1079 cm^{-1} corresponds to band D_4.

The higher intensity of the G band results from the diminishing volatile content in the waste material. Besides that, during the thermal degradation process, when high temperatures are reached, a reorganization of the lignocellulosic structures into polychromatic ones occurs, which leads to the formation of carbon crystallites, allowing the G band to be dominant. The G band, which is this carbonaceous structure, is

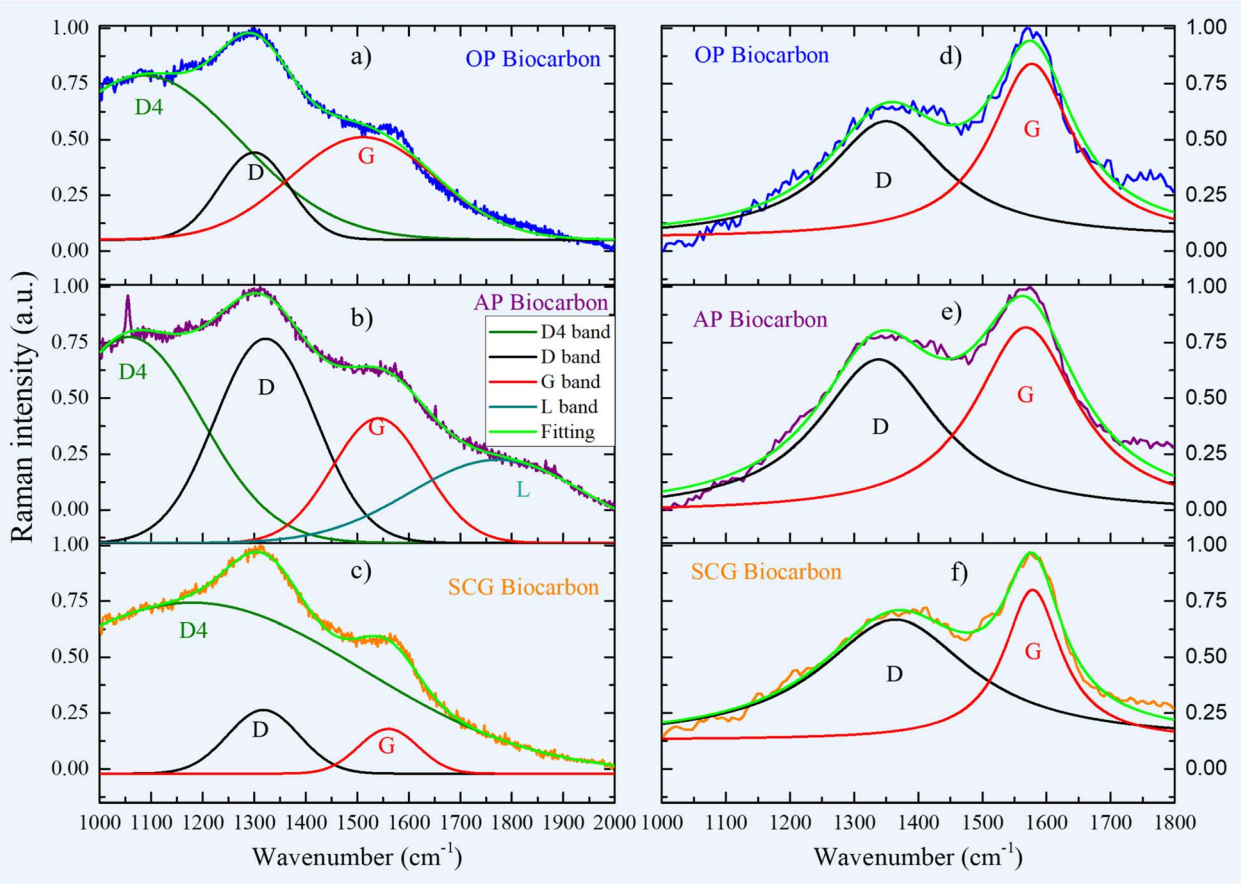

Fig. 4 Lorentzian fitting of the first order Raman spectra. (a)–(c)-Raman fitting of the spectra for the OP, AP and SCG-derived biocarbon samples from the TGA calorimeter; (d)–(f)-Raman fitting of the spectra for the OP, AP and SCG biocarbon samples obtained in a high-temperature furnace.

mainly attributed to the aromatic rings and to the carbon crystallites as a result of the carbonization of the organic biomass. The presence of only the D and G bands in the spectrum of the biocarbon from the high-temperature furnace indicates that the material is composed of partially ordered sp^2-hybridized carbon atoms.

Raman results of the furnace-biocarbon. Fig. 4d–f correspond to the Raman analysis for the OP-BC, AP-BC, and SCG-BC, respectively, when the thermal degradation of the raw wastes was made in a high-temperature furnace, carrying out the process at 350 °C. Actual pictures of these biocarbon samples can be observed in Fig. 1b. This analysis was conducted to scale the production of waste biomass-derived biocarbon, which will serve as the raw material for producing carbon nanodots, as shown later. As observed, the Raman signals of the three samples are similar to each other, but different from those recorded for the biocarbon from the TGA analysis. The performed Lorentzian fitting allowed for the very good identification of only the D and G Raman bands, as the three fitting peaks were not allowed. As observed, the intensity of the D and G bands for the biocarbon derived in the furnace is inverted compared to those obtained in the TGA calorimeter. The ratio of the intensities of the I_D/I_G for the three biocarbon samples was in this case 0.87 (OP-BC), 0.91 (AP-BC), and 0.90 (SCG-BC), which indicates the presence of disordered carbon, as these are less than 1. For the OP-BC, the D and G bands were identified at 1350 cm^{-1} and 1577 cm^{-1}, respectively, while for the AP-BC and SCG-BC, those were at 1338 cm^{-1} and 1568 cm^{-1}, and 1364 cm^{-1} and 1578 cm^{-1}, correspondingly. These results confirm that the thermal treatment in a high-temperature furnace produces biocarbon with a consistent degree of structural disorder across the different biomass sources, as evidenced by the comparable I_D/I_G ratios below 1. The inversion of D and G band intensities relative to the TGA-derived biocarbon highlights how the synthesis route significantly influences the carbon structure.

SEM-EDS analysis of the furnace-derived biocarbon. SEM micrographs in Fig. 5 illustrate the structural characteristics of the biocarbon derived from each biomass because of their thermal degradation in the furnace. The OP-BC micrograph is shown in Fig. 5a, AP-BC in Fig. 5b, and SCG-BC in Fig. 5c. The OP-derived biocarbon exhibits a highly porous and irregular structure. In contrast, the biocarbon obtained from AP and SCG displays hexagonal-like porous structures. Fig. 5d presents a magnified micrograph of a pore in the SCG-BC, revealing a cylindrical morphology with an approximate diameter of 50 microns. Fig. 5e, f, and 5h also correspond to the micrographs of OP-BC, AP-BC, and SCG-BC obtained from the high-energy

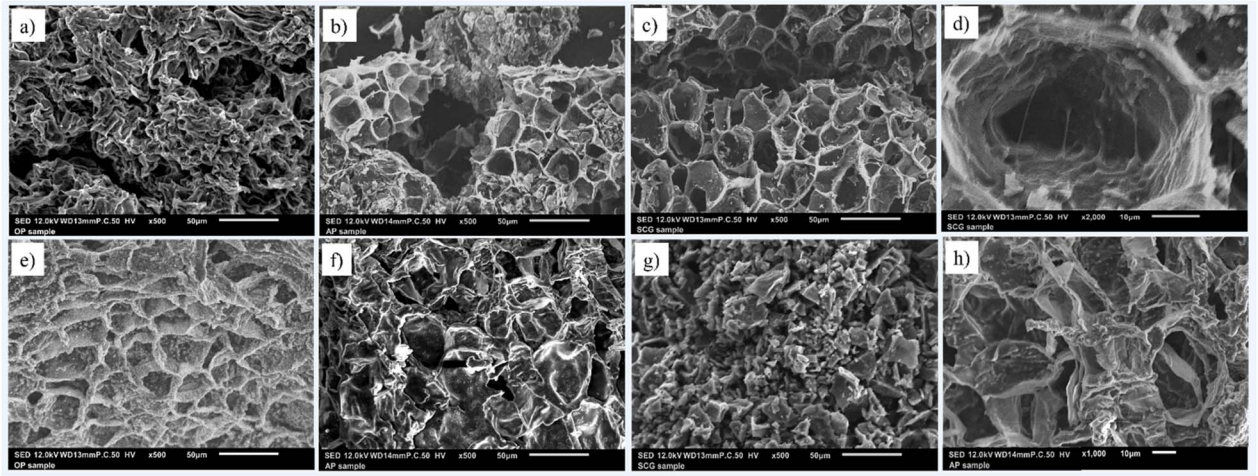

Fig. 5 SEM micrographs for the biocarbon obtained in the TGA calorimeter and the high energy furnace, (a)-OP biocarbon, (b)-AP biocarbon and (c)-SCG biocarbon from TGA; (d)-is a zoom of a hexanal-shaped pore for the SCG-biocarbon; (e)–(g) are for the OP, AP and SCG biocarbon from the furnace, respectively; (h) zoom for the AP biocarbon to observe the porous shapes.

furnace, respectively. While these biocarbons exhibit similar porosity, the structural characteristics of the pores differ. The SCG-BC lacks the well-defined porous features observed in the other two samples. However, no significant structural differences are evident between the biocarbons.

SEM micrographs reveal the porous structure of the synthesized biocarbon, with no significant morphological differences between them, maintaining their porosity in both TGA- and furnace-derived structures. The chemical composition of the biocarbon from the furnace was analyzed using EDS to determine its elemental composition. Table 1 summarizes the mass percentages of each biocarbon, including those recovered from the TGA calorimeter at a maximum temperature of 800 °C and those produced in the furnace at 350 °C (blue columns). As expected, carbon (C) constitutes the highest percentage in both cases, followed by oxygen (O), reflecting the carbon-rich nature of the waste-derived biocarbon. All three biocarbons predominantly contain C, O, potassium (K), and phosphorus (P), while the OP-BC sample exhibits a notably high calcium (Ca) content (5.79%). The AP-BC sample presents a lower carbon content but the highest oxygen concentration among the three. Additionally, OP-BC and AP-BC exhibit higher potassium levels compared to SCG-BC, while all three biocarbons contain only trace amounts of P, magnesium (Mg), and sulfur (S). These elemental compositions align with the known chemical constituents of their respective biomass sources.

Regarding the biocarbon obtained from the furnace, some compositional differences were observed compared to those derived from the TGA analysis. The AP-BC exhibited an even lower carbon content and the highest oxygen mass percentage; however, its oxygen content was slightly lower than its potassium content (23.13%). This aligns with the well-known high potassium content of avocados. The low carbon percentage and high oxygen concentration in AP-BC may be attributed to the partial degradation of lignin and contributions from cellulose and hemicellulose decomposition. Furthermore, the high potassium content could originate from residual pulp on the peels, as they were used without cleaning after consumption. Avocados can contain up to 0.95 g of potassium per 100 g of pulp. The partial degradation of lignin likely results in poorly structured biocarbon (amorphous carbon) with a high concentration of oxygen-functionalized groups and associated potassium compounds.

Table 1 Mass percentage of the thermally derived BC from the TGA calorimeter and high-energy furnace obtained through EDS analysis

Mass percentages (%)						
	OP-BC		AP-BC		SCG-BC	
Element	TGA	Furnace	TGA	Furnace	TGA	Furnace
C	73.96	72.79	68.02	52.53	84.77	80.85
O	16.43	16.62	18.82	20.21	9.28	16.07
K	3.43	9.91	11	23.13	2.93	1.34
P	0.19	0.36	0.79		0.93	0.46
Mg	0.20		0.51		0.90	0.55
Ca	5.79				1.19	0.53
S		0.22				0.19
Cl		0.42		1.71		
Al				1.49		
Cu				0.92		
Total	100%					

Carbon nanodots

Morphological analysis through TEM and HRTEM. The different biocarbons described in Fig. 5 were utilized as raw carbonaceous materials for the pulsed laser-assisted synthesis of CNDs. The CNDs were synthesized in water, and, unlike raw biocarbon, stable colloidal suspensions of CNDs were obtained following laser-induced ablation/fragmentation. The resulting colloidal suspensions are shown in the actual image in Fig. 1d. Quantifying the yield of carbon nanodots (CNDs) from different synthesis routes remains challenging. In this study, an

approximate yield was estimated from the weight differences of the residual, non-fragmented biocarbon after laser fragmentation. For each sample, 4 mL of the CND-containing colloid was carefully removed, and the remaining solid residue was collected and dried. The dried residues were deposited on pre-weighed glass slides using an analytical balance with a precision of 0.0001 g (Thermo-Fisher). Samples were then oven-dried at 75 °C for 48 hours, yielding final residue weights of 0.092 g, 0.090 g, and 0.094 g for the OP-CNDs, AP-CNDs, and SCG-CNDs, respectively. These values suggest approximate yields of 8%, 10%, and 6%. However, these results should be interpreted with caution, since the initial colloidal suspensions had nearly identical masses (4.03 g each). Notably, the higher apparent yield of AP-CNDs may reflect their greater production of smaller (~2 nm) CNDs, yet the contribution of larger nanostructures—also observed in TEM micrographs—likely influences the overall colloidal mass. Therefore, in this context, "yield" should be understood as the efficiency of generating stable, ultrasmall CNDs, rather than solely the fraction of fragmented biocarbon. Further quantitative analyses will be required in future work to more accurately assess CND production efficiency and for the scalability process.

To characterize the type of nanostructured carbon-based materials resulting from the pulsed laser interaction with the water-suspended biocarbon micro-powders, TEM and HRTEM micrographs of the products are presented in Fig. 6, 7, and 8. Fig. 6 displays TEM micrographs of the nanostructures derived from the OP-BC. Large particles with sizes around 30 nm were observed, as shown in the upper micrographs, alongside near-spherical and irregularly shaped particles. Nanostructures (lower micrographs) with sizes ranging between 4 and 10 nm (marked with black borders), which can be classified as carbon nanodots (OP-CNDs).

HRTEM analysis further revealed interplanar distances of the crystalline carbon nanostructures produced, approximately 0.335 nm (highlighted with yellow lines), corresponding to the (002) graphite plane of graphite.[61] This distance is associated with the spacing between graphene layers in the graphite structure. In the final micrograph, a cluster of four OP-CNDs was observed, three exhibiting an interplanar distance of

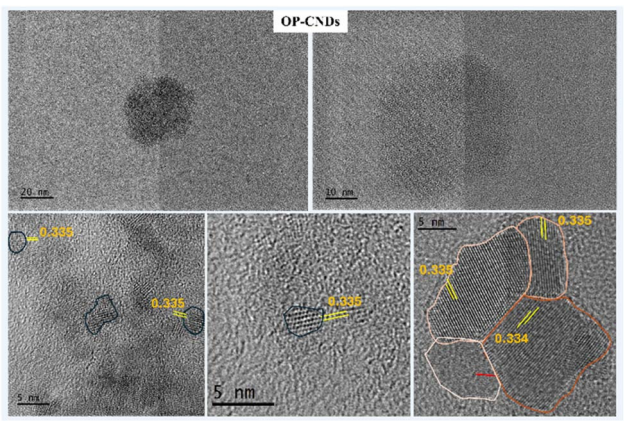

Fig. 6 TEM and HRTEM of the OP-CNDs.

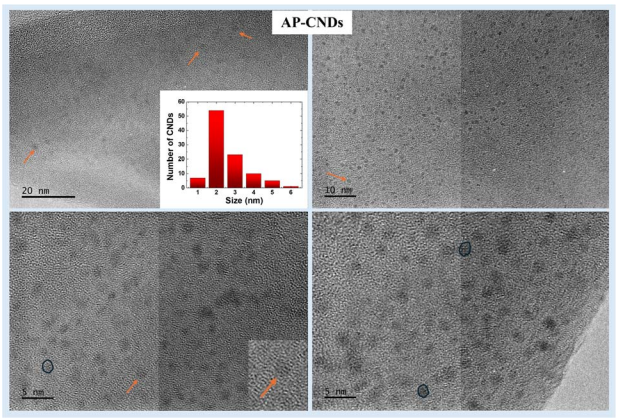

Fig. 7 TEM and HRTEM of the AP-CNDs.

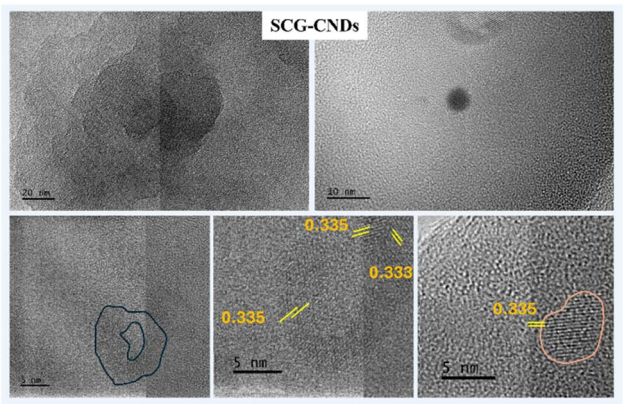

Fig. 8 TEM and HRTEM of the SCG-CNDs.

0.335 nm, consistent with the already mentioned (002) plane. However, the fourth nanostructure exhibited a smaller interplanar distance, approximately 0.212 nm (red line), which can be attributed to the (100) plane of graphite, associated with the in-plane spacings of the honeycomb lattice of carbon atoms.[62] This inter-plane distance has been attributed to the case of AA-stacking in graphite, which is rare. Still, it has been experimentally observed only in some specifically treated samples of graphite.[63] From the obtained micrographs, it was not possible to build a histogram of the produced OP-CNDs and related nanomaterials. Nonetheless, these results demonstrate the successful synthesis of carbon nanodots using OP waste-derived biocarbon as raw materials.

The nanostructured materials obtained after the pulsed laser ablation of the AP-BC were found to be entirely different from those derived from the OP-BC. Fig. 7 displays TEM micrographs showing very small particles, with sizes less than 5 nm, identified as AP-CNDs. In the upper two micrographs, where the scales are 20 nm and 10 nm, the CNDs appear as dark grey dots, some highlighted with orange arrows. In the lower micrographs, predominantly spherical CNDs are observed, with sizes below 5 nm. The inset shows a histogram constructed from accounting of 100 CNDs, indicating an average size of 2.3 nm;

this type of histogram was impossible to determine in Fig. 6 for the OP-CNDs.

HRTEM micrographs reveal that the produced CNDs are composed of amorphous carbon, as no interplanar distances could be identified. This is evident in the zoomed-in view of a CND highlighted with an orange arrow in the third micrograph. The absence of crystalline planes confirms the amorphous nature of these nanostructures. Such nanostructures are typically classified as amorphous CNDs, characterized by the lack of a well-defined crystal lattice. They predominantly consist of a mixture of sp^2 (graphite-like) and sp^3 (diamond-like) hybridized carbon, along with a significant presence of dangling bonds and surface functional groups, which contribute to their unique properties.[64,65] According to the laser ablation process, many CNDs obtained from the BC can be attributed to their poorly structured biocarbon, which maximizes the ablation process.

Some micrographs of the carbon-based nanostructures produced from the fragmentation of the SCG-BC are presented in Fig. 8. TEM micrographs revealed large and non-uniform particles, as shown in the upper micrographs, from which spherical particles with a size of less than 10 nm were captured. HRTEM images allowed the observation of near-spherical structures, with a diameter of between 5 and 10 nm, with a crystalline structure whose interplanar distances are 0.335 nm, corresponding again to the (002) plane of graphite.[61] Similar to the OP biocarbon, the SCG biocarbon yields crystalline nanostructures, which can also be considered as SCG-CNDs. However, in this case, a very low abundance of this type of carbon nanodots was observed, which can be related to a low efficiency in the ablation process.

The pulsed laser fragmentation of waste-derived biocarbon allowed obtaining carbon-based nanostructures, mainly crystalline and amorphous carbon nanodots. The avocado peel led to smaller and amorphous CNDs. Several reasons could be responsible for these observations. For example, AP typically has a high carbon content due to its rich organic matrix, including polysaccharides, lipids, and lignin. The pyrolysis process could yield BC with a higher density of amorphous carbon, making it more susceptible to laser-induced ablation/fragmentation, yielding the amorphous observed CNDs and the highest concentration. Then, the higher carbon content of OP-BC and SCG-BC, as shown in the EDS results, could lead to a more uniform biocarbon structure. On the other hand, OP, with higher pectin content, and SPG, with a complex lignocellulosic structure, may result in biocarbon with more crystalline or rigid characteristics, which are less responsive to laser-induced fragmentation. These could explain the observed crystalline OP-CNDs and SCG-CNDs.[43,45]

Similarly, it is well-known that lignin is a complex aromatic polymer that contributes to rigidity and thermal stability in biomass. OP and SCG contain higher lignin content than AP, resulting in BC with a high content of rigid aromatic structures less prone to laser ablation. In contrast, with lower lignin content, AP yields biocarbon with a more amorphous and disordered structure (see Fig. 5), making it easier to fragment into CNDs. The efficiency of AP-BC ablation into amorphous CNDs is likely due to its lower ash content, possible lipid-derived carbon structures, higher hydrophilicity, and more amorphous carbon regions.[43,46,49] These factors collectively enhance the interaction with laser pulses in water, forming smaller, well-defined CNDs compared to biocarbon derived from OP-BC and SCG-BC. However, additional factors can be present.

Optical properties of the CNDs aqueous suspensions. The optical properties of the CNDs in aqueous suspension were initially examined using UV-Vis absorbance spectroscopy, with the corresponding absorbance spectra presented in Fig. 9a. The spectra did not exhibit distinct absorption bands for each CND suspension, but rather differences in absorbance intensity. Among the samples, the OP-CND suspension displayed the highest absorbance. In contrast, the SCG-CND suspension exhibited the lowest, which correlates with the visual appearance of the samples shown in Fig. 1d. As observed in the absorbance spectra, this kept the typical shape for carbon-based material, with the large absorbance between 300–400 nm, which is normally assigned to the $n \rightarrow \pi^*$ transition of the C=O bond in carbon cores.[66] Below 300 nm, the $\pi \rightarrow \pi^*$ transition implying aromatic sp^2 carbons (aromatic C=C bonds) appears to be responsible for the electronic transitions, and normally are presented as well-defined bands,[66,67] which are not observed in this study.

The light emission properties of the CND suspensions were recorded under various excitation wavelengths using photoluminescence (PL) spectroscopy. The PL response varied among the different CND types, as shown in Fig. 9b (OP-CNDs), 9c (AP-CNDs), and 9d (SCG-CNDs). Notably, the AP-CNDs exhibited the highest PL intensity, followed by OP-CNDs, while SCG-CNDs displayed the weakest recorded emission; this response can be associated with the large amount of produced CNDs, as micrographs in Fig. 7 revealed. The PL response was found to be excitation-wavelength-dependent, with maximum emission intensities observed when excited at 330 nm and 350 nm. SCG-CNDs exhibited low emission, well-detectable only under 330 nm excitation (Fig. 9d). In contrast, AP-CNDs maintained photoluminescence even when excited at longer wavelengths, such as 470 nm and 490 nm (Fig. 9c). The inset in Fig. 9b further highlights the PL intensity under 330 nm excitation, clearly demonstrating the PL response differences among the three CND suspensions.

Additionally, preliminary quantum yield (QY) measurements were carried out for the three samples using an excitation wavelength of 330 nm, since all of them exhibited a detectable photoluminescence response under this condition. The inset in Fig. 9c shows the calculated QY values: 5.313% for OP-CNDs, 4.844% for AP-CNDs, and only 0.536% for SCG-CNDs. These results indicate that the light-to-emission conversion efficiency of SCG-CNDs is very low, whereas OP-CNDs exhibit the highest efficiency among the tested samples. The quantum yield of the CNDs (QY_{CNDs}, %) was calculated following previously reported methods for CNDs,[68–70] using quinine sulphate (QS) in 0.1 M H_2SO_4 as the reference standard, with a well-known QY_{QS} of 54%. Since the CNDs were dispersed in water, a refractive index

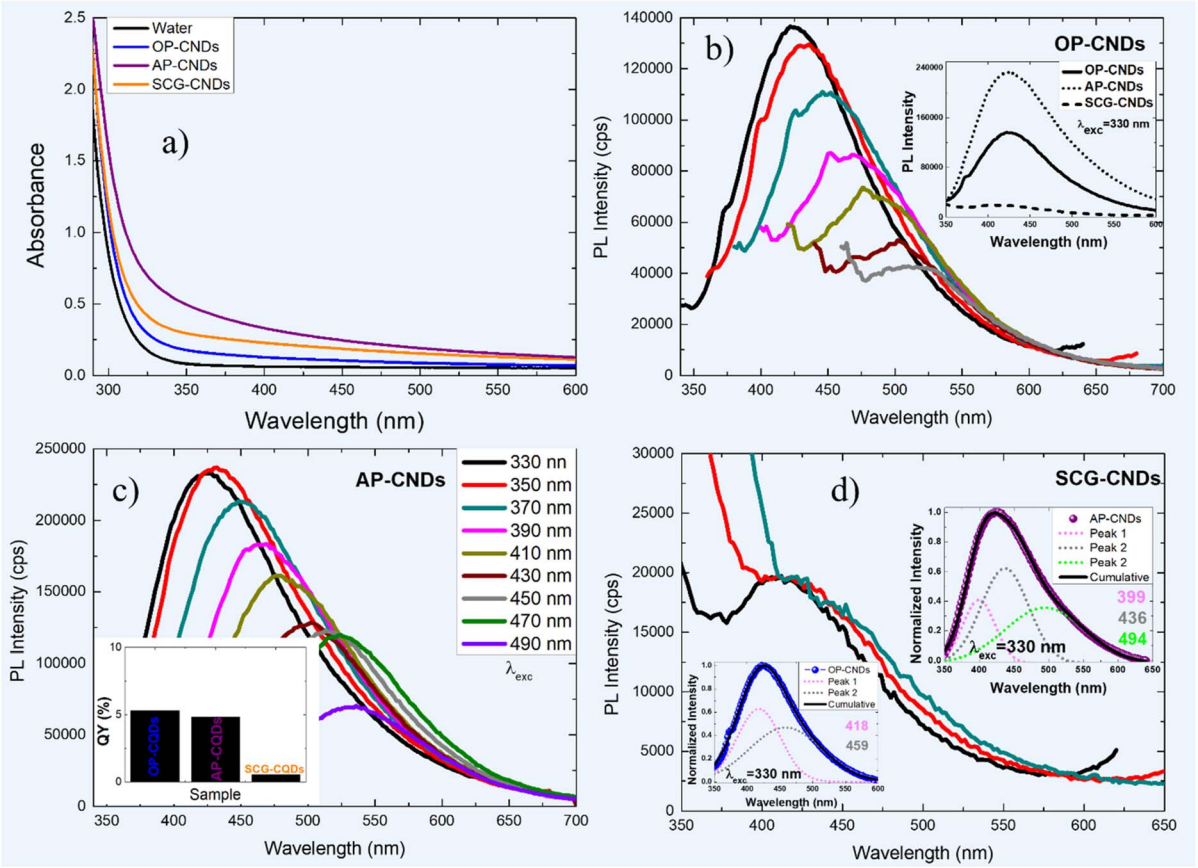

Fig. 9 Optical properties of the prepared CNDs, (a)-Absorbance spectra of the three carbon nanodots samples. (b) PL spectra of the OP-CNDs suspensions, (c) AP-CNDs and (d) SCG-CNDs.

of 1.33 was used. The calculations were performed using the standard equation:

$$QY_{CNDs} = QY_{QS}\left(\frac{A_{CNDs}}{A_{QS}}\right)\left(\frac{PL_{CNDs}}{PL_{QS}}\right)\left(\frac{n_{CQDs}}{n_{QS}}\right),$$

where A_{CNDs} is the absorbance for the CQDs samples at 330 nm and A_{QS} is for reference, which was, as in ref. 68, diluted in 0.1 M H_2SO_4. PL is the integrated emission curve for the sample and reference. Here, n_{QS} was 1.33. Table 2 summarizes the acquired data for the quantum yield calculations. The QY of carbon dots has been widely reported, showing strong dependence on the synthesis route and processing conditions, including temperature, reaction time, surface features, and precursor composition. For instance, nitrogen-doped carbon dots (N-CDs) prepared by an ultrasonication method[71] achieved a QY of 27%. In contrast, significantly higher values, such as 60.7%, have been reported for N-CDs synthesized *via* a microwave-assisted process.[72]

Table 2 Data for QY calculations for the three CNDs samples

	OP-CNDs	AP-CNDs	SCG-CNDs
A_{CNDs}	0.109	0.107	0.102
A_{QS}	0.103	0.103	0.103
PL_{CNDs}	60 507	56 206	6575
PL_{QS}	650 801	650 801	650 801
QY_{CNDs}	5.313	4.844	0.536

The QY of the OP-CNDs was the highest; however, the maximum emission intensity, as shown in Fig. 9b and c, was observed for the AP-CNDs sample. This discrepancy can be attributed to the larger concentration of CNDs in the avocado-derived system, reflected in its higher absorbance. Therefore, the stronger PL signal of AP-CNDs is primarily a concentration effect rather than a consequence of higher quantum yield.[73] This suggests that laser fragmentation of AP-BC is more efficient than that of OP-BC, producing a greater abundance of CNDs and, consequently, more emissive centers. For comparison, for example, it has been reported that *E. prolifera* can be converted into fluorescent CNDs *via* a one-pot green hydrothermal process,[69] yielding QYs of 1.2–7.1%, values close to those reported in this study. In that work, impurities such as crude proteins, lipids, and inorganic salts were identified as contributors to the low QY, which is consistent with the IR analysis presented here and discussed in detail in the following section. Similarly, carbon quantum dots (CQDs) derived from wholemeal bread, soybean flour, and lemon juice exhibited a QY of 2.31%. On the other hand, CNDs synthesized from ethylenediamine (E-CNDs) or urea (U-CNDs) in a single-step microwave process[74] showed markedly different QYs of 64.0% and 8.4%, respectively. The results obtained here from laser

fragmentation of organic waste-derived biocarbon, therefore, show similar behavior to biomass-derived CNDs produced by other methods. However, the preparation routes differ in terms of synthesis conditions and efficiency, as highlighted earlier.

The inset in Fig. 1d presents an actual photograph of the CND suspensions under a 350 nm UV lamp in a dark environment, superposed to the ones under white light, revealing their characteristic blue-green photoluminescence. The AP-CNDs and SCG-CNDs suspensions exhibit a similar coloration with a weaker emission than the AP-CNDs suspension. The insets in Fig. 9d illustrate the decomposition of the PL spectra through multi-peak analysis, fitted with Gaussian curves. The lower inset displays the PL spectrum of the OP-CNDs suspension under 330 nm excitation, which can be well-fitted with two Gaussian peaks centered at 418 nm and 459 nm (dashed curves). The upper inset corresponds to the AP-CNDs suspension under the same excitation wavelength, where a three-peak fitting analysis identifies emission peaks centered at 399 nm, 436 nm, and 496 nm (dashed curves). The FWHM for each PL spectra was 103.85 nm for the OP-CNDs and 114.12 nm for the AP-CNDs. These results indicate the polydispersity of the CND suspensions, leading to the observed broad emission band, which is typical in these CND systems.

IR analysis: origin of the PL response. The multi-peak fitting of the PL spectra for the CNDs suspensions in Fig. 9 can be interpreted as the result of a combination of light-emitter centers with different wavelengths, mostly composed of ones emitting at 399 nm, 436 nm, and 494 nm, with those whose emission is centered at 436 nm being more abundant. To insight the origin of the PL response of the as-prepared CNDs, an IR analysis of the biomass OP, AP, and SCG was conducted. The same analysis was made for biocarbon, OP-BC, AP-BC, and SCG-BC, and their corresponding produced CNDs.

For the biomasses, the recorded IR bands are presented in Fig. 10a, from which the three samples have mostly the same IR signal, with some shifting and intensity variations. Concerning the high frequency region (green rectangle), the broad and strong band around 3315 cm^{-1} is attributed to the O–H stretching vibrations of hydroxyl groups, commonly found in cellulose, hemicellulose, and lignin.[75] These hydroxyl groups are responsible for the hydrophilic nature of the biomass and are involved in extensive hydrogen bonding. This band was found to be more intense for the OP-biomass due to its containing more pectin and free phenolic compounds. The 2920 cm^{-1} and 2854 cm^{-1} bands correspond to asymmetric and symmetric stretching vibrations of aliphatic C–H bonds, primarily from CH_2 and CH_3 groups present in cellulose, fatty acids, and waxy cuticular components.[75,76] These could be noticeable in OP and AP due to their lipid and wax content.

The weaker IR bands, in the mid-IR region (orange rectangle), at 2370 cm^{-1} and 2320 cm^{-1} are often attributed to atmospheric CO_2. Still, in biomass they may also relate to C≡C or C≡N groups in trace components or degradation products.[77,78] The band at 2154 cm^{-1} could indicate the presence of nitriles (C≡N) or cumulene-like structures, which can form during partial decomposition of lignin.[79] The signal at 2015 cm^{-1} may arise from overtones or combination bands or

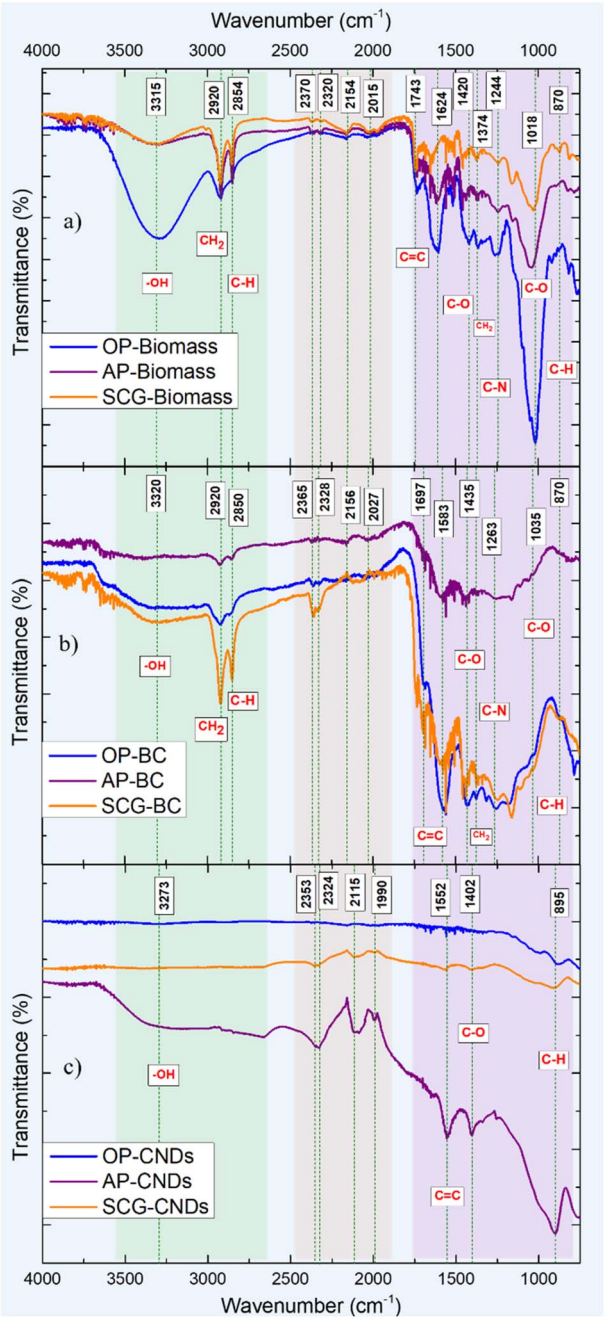

Fig. 10 IR spectra of the OP, AP and SCG (a)-biomasses, (b)-biocarbon and (c)-CNDs.

could suggest weak conjugated systems.[80] The band at 1743 cm^{-1} is attributed to C=O stretching vibrations of ester and carboxylic acid groups, which are highly abundant in pectin and hemicellulose.[75] This band is particularly strong in OP due to its high pectin content and noticeable in AP. The 1624 cm^{-1} band corresponds to aromatic C=C stretching (from lignin structures) or could also be attributed to conjugated carbonyl (C=O) or amide bands in residual proteins.[75–77] Finally, in the fingerprint IR interval (purple rectangle), the bands at 1420 cm^{-1} and 1374 cm^{-1} can be assigned to CH_2 scissoring and bending vibrations, related to lignocellulosic

backbones.[75,76] The 1244 cm^{-1} band may arise from C–O stretching of esters or ether linkages, particularly in lignin and hemicellulose. The 1018 cm^{-1} band is strongly associated with C–O–C and C–OH stretching in polysaccharides such as cellulose and hemicellulose, and is present in all three samples.[75] The signal at the 870 cm^{-1} band is often linked to aromatic C–H out-of-plane bending, found in lignin, or can also indicate glycosidic linkages in sugars.[81]

As can be seen in Fig. 10b, most of the IR bands for the biomasses are present, which can be explained by the fact that the thermal degradation (slow pyrolysis) at 350 °C is partial and does not fully remove all organic functional groups. The persistence of these IR bands indicates that the produced biocarbon is chemically active, retaining surface functional groups that can be useful for further applications, *i.e.*, adsorption, catalysis, or nanomaterial precursors.[82] At higher temperatures (500–700 °C), it would likely reduce or eliminate many of these bands due to increased aromatization and deoxygenation, forming more graphitized carbon structures. For example, functional groups such as hydroxyl (–OH), carbonyl (C=O), and aliphatic C–H can survive or partially degrade into intermediate structures.[83] At 350 °C, lignin starts to break down slowly. Still, aromatic structures and some phenolic groups remain intact, which accounts for the bands like 1583 cm^{-1} or 1697 cm^{-1} for aromatic C=C or conjugated C=O stretch, while the ones at 870 cm^{-1} show the aromatic C–H out-of-plane bending.[75,83] To end, some bands could not directly arise just from the biocarbon structure, but from adsorbed CO_2 or other gases. Triple bonds or conjugated systems formed as intermediates could be responsible for the bands at 2154 cm^{-1} and 2015 cm^{-1}, possibly from nitriles (C≡N), as has been mentioned above.[83,84] This is more possible as here the biomass has already been degraded by the thermal treatment.

In Fig. 10c, the IR signal of the laser-produced CNDs is presented. As observed, not all the IR signals for the previous systems were retained in the nanomaterials produced. The signal related to –OH groups was well-recorded only for the AP-CNDs, besides the ones for the C=O, C–O, and C–H, as seen in the purple line. These signals can also be observed for the SCG-CNDs, with no significant response for the AP-CNDs. As observed in Fig. 6, the AP-CNDs showed more abundance, which has been related to the highest PL intensity. The C=C bonds are commonly found in graphitic domains or partially aromatic rings formed during the carbonization of biomass. This suggests that the carbon structure retains some aromatic or conjugated character, which is often responsible for the optical activity of CNDs.[83,85] Laser ablation is a fast and localized process, but not all functional groups are broken. This could lead to spontaneous surface functionalization due to reactive species[86] in solution (oxygen, water). These functional groups are essential for photoluminescence and solubility,[85] which can be related to the AP-CNDs' photoluminescence behavior.

The recorded functionalized groups affect the electronic structure and surface chemistry, influencing how CNDs absorb and emit light. In CNDs, the emission is mostly attributed to these types of groups, more than from quantum confinement, as in carbon quantum dots. The C=C bonding contains sp^2-hybridized carbon domains, often the primary origin of absorption in the UV region, and could contribute to intrinsic photoluminescence. Even when no specific band absorption band was observed, the $\pi \rightarrow \pi^*$ has been reported in CNDs around 340 nm and is present in C=C bonds.[87] These conjugated regions act like molecular fluorophores, where excitation of π electrons leads to radiative recombination. The oxygen-containing groups, –OH and C–O, are mostly on the surface and can introduce surface defect states that can act as trap states for electrons or holes.[88] The PL response in CNDs is an intricate physicochemical process; however, the observed results provide insights into their origin in the produced carbon nanodots from laser-ablated waste-derived biocarbon.

XPS results. The XPS spectra of the samples revealed four main carbon-related peaks, as shown in Fig. 11a–c. For the OP-CNDs, distinct signals were observed at 154.2, 284.1, 399.1, and 532.4 eV, corresponding to S 2p, C 1s, N 1s, and O 1s, respectively.[89,90] In contrast, the S 2p signal was absent in the AP-CNDs and SCG-CNDs. For these two samples, the C 1s, N 1s, and O 1s signals were recorded at comparable energies: 284.1, 400.1, and 531.0 eV for the AP-CNDs, and 284.1, 401.0, and 532.2 eV for the SCG-CNDs. Additionally, an extra feature at ~978.0, 977.2, and 976.6 eV was detected for the OP-, AP-, and SCG-CNDs, which is attributed to the Na 1s signal. Overall, these results confirm that the three CND samples are primarily composed of carbon, nitrogen, and oxygen, with a minor contribution of sodium. At the same time, only the orange-peel-derived CNDs contain detectable sulphur.

F The deconvoluted C 1s spectra for the three CND samples (Fig. 11d–f) reveal both common and distinctive features depending on the biocarbon source. For the OP-CNDs, three main peaks were observed at 283.13, 284.27, and 285.50 eV. The low-binding-energy peak at 283.13 eV can be attributed to carbide-like bonding[91] associated with residual inorganic elements (*e.g.*, Mg and Ca) present in the orange peel biocarbon, as supported by EDS analysis (Table 1). The peak at 284.27 eV corresponds to C–C bonding,[89] while the one at 285.50 eV is likely related to C–S interactions,[89] or sp^3 (C–C, and C–H) surface funtionalities.[92] In the case of the AP-CNDs, five components were identified: a carbide-like peak[91] at 283.55 eV (also linked to residual Mg), a signal at 284.84 eV assigned to sp^2 carbon (C=C), and a peak at 285.76 eV associated with C=O bonding. Additional contributions include a feature at 288.02 eV, attributable to C=O/C=N functionalities,[89] and a shake-up satellite at 291.84 eV, characteristic of $\pi \rightarrow \pi^*$ transitions in aromatic sp^2 carbon systems, typically observed in graphitic domains.[93] For the SCG-CNDs, the spectrum exhibited a carbide-related peak at 283.41 eV, again arising from inorganic Mg and Ca residues, along with features consistent with sp^2 carbon at similar energies to those found in the OP-CNDs. A distinct contribution at 286.16 eV was assigned to C–N bonding,[91,93] suggesting nitrogen incorporation into the carbon framework. Together, these results demonstrate that while all three CND systems share signatures of sp^2-hybridized carbon and carbide-related features, additional functional groups such as C–S in OP-CNDs, C=O/C=N in AP-CNDs, and

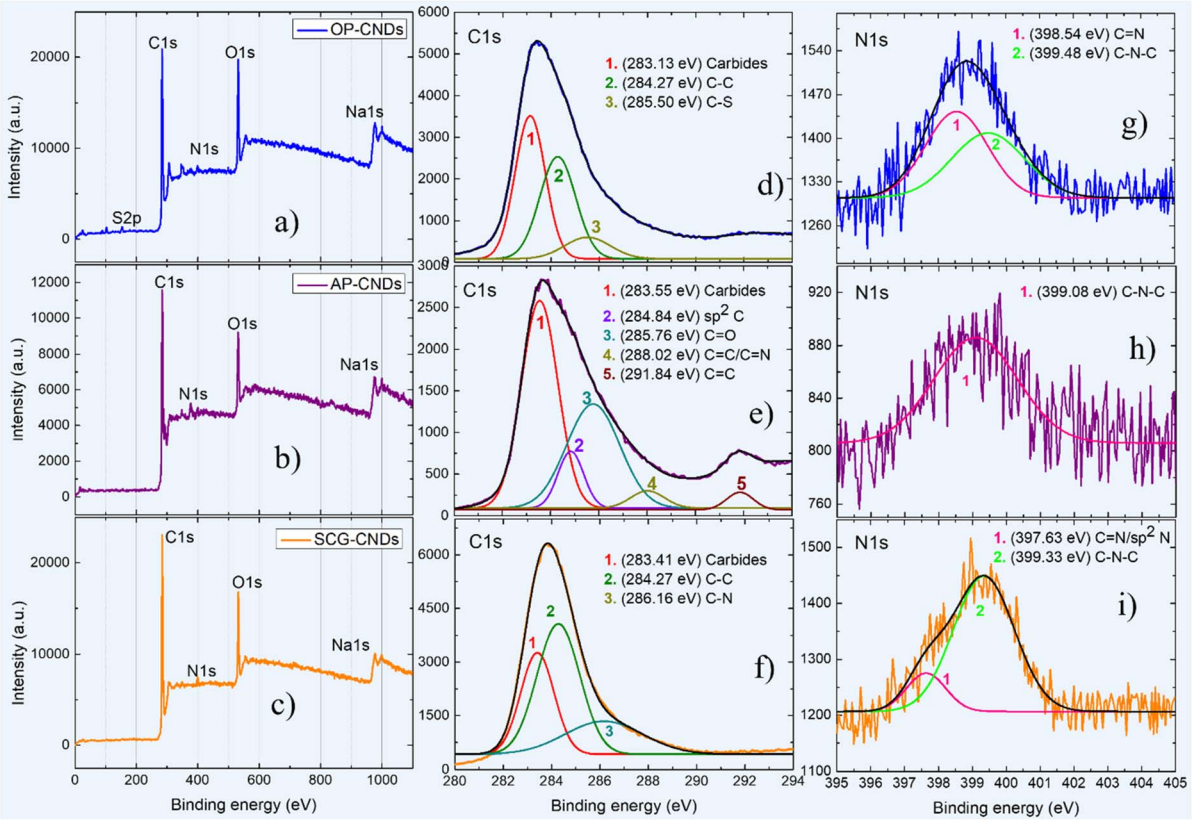

Fig. 11 Survey XPS spectrum for the (a) OP-CNDs, (b) for AP-CNDs and (c) SCG CNDs. Deconvolution of the C 1s spectra for (d) OP-CNDs, (e) for AP-CNDs and (f) SCG CNDs; and for the N 1s, (g)–(i) for OP-CNDs, AP-CNDs and SCG CNDs, respectively.

C–N in SCG-CNDs reflect the chemical complexity of the different biomass precursors.

Fig. 11g–i present the deconvoluted N 1s spectra for the three CND systems. For the OP-CNDs (Fig. 11g), two peaks were resolved at 398.54 and 399.48 eV, which can be attributed to C═N bonding and C–N–C surface components,[89,92] respectively. In contrast, the AP-CNDs sample (Fig. 11h) exhibited only a single peak centred at 399.08 eV, assigned to C–N–C groups.[89] Finally, the SCG-CNDs (Fig. 11i) displayed two contributions at 397.63 and 399.13 eV, which were assigned to C═N or sp^2-hybridized nitrogen species, and to C–N–C surface functionalities,[92] respectively. These results suggest that nitrogen incorporation depends strongly on the biomass precursor, with SCG-CNDs exhibiting the broadest variety of nitrogen-related chemical surfaces.

The combined XPS, IR, and PL analyses reveal that the photoluminescence of the waste-derived CNDs is an intricate process and originates primarily from the interplay between sp^2 carbon domains and surface functional groups introduced by the biomass precursors. XPS confirmed a common carbon–nitrogen–oxygen content across all samples, with precursor-specific functionalities such as C–S (OP-CNDs), C═O/C═N (AP-CNDs), and C–N (SCG-CNDs), which correlate with the IR-identified residues of hydroxyl, carbonyl, and aromatic groups retained after pyrolysis. These surface functionalities, as has already been discussed, act as defect states and emissive centers, complementing the intrinsic $\pi \rightarrow \pi^*$ transitions of sp^2 domains. Overall, the results highlight that both the carbon framework and the functional groups preserved from the biomass precursors drive the observed structural and optical features.

TRPL spectroscopy results. Fig. 12 contains the TRPL results for an excitation wavelength of 350 nm, with a pulse duration of 10 ns, as previously described. The emission was recorded for the three CND suspensions at three different wavelengths: 410 nm (Fig. 12a), 435 nm, which corresponds to the maximum wavelength emission in Fig. 9 (Fig. 12b), and 540 nm, whose response is presented in the inset in Fig. 12b under the same excitation wavelength. As observed, the light emission of the AP-CNDs exhibits fast delay times, 1–2 ns, which are slightly larger than those of the other samples, around four ns, when the emission is recorded at 410 and 435 nm. As observed in the inset of Fig. 11b, the delayed time for the emission at 540 nm is larger than that of the previous one, and it can be identified as 6–7 ns. Similar results have been reported for CNDs produced using the same laser system but using carbon black as a carbon source.[18] The recorded results indicate that the 100 ns pulse allowed a PL response whose intensity is always higher for the AP-CNs than the other two suspensions, which agrees with the amount of nanodots, as has been discussed, considering the large emission for the PL results in Fig. 9. As can be seen in the inset of Fig. 12b, the resolved spectra for the emission at 540 nm

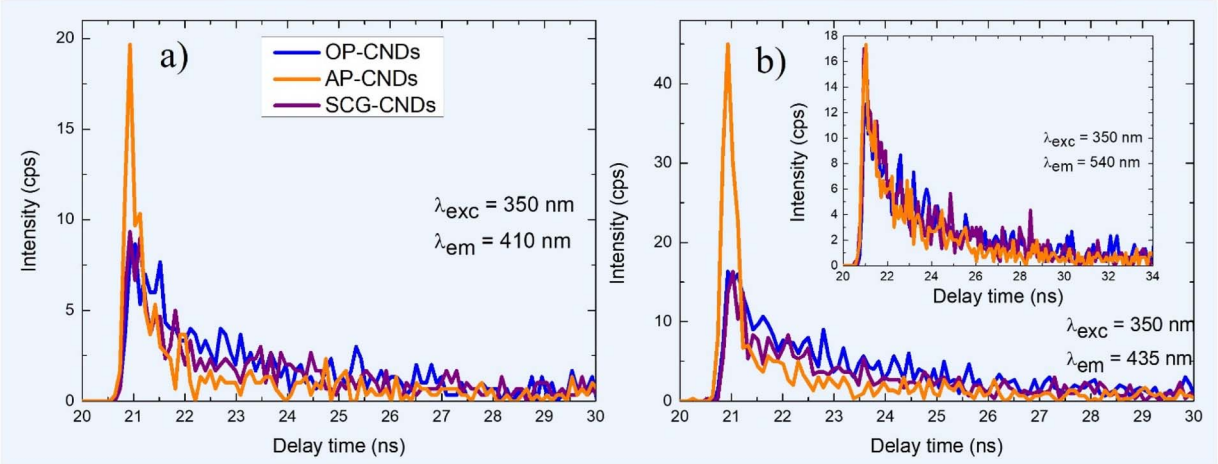

Fig. 12 TRPL spectra of the OP (blue line), AP (orange line) and SCG (purple line) using an excitation wavelength of 350 nm with 100 ps pulse duration, recording the emission at (a)—410 nm, (b)—435, and 540 nm (inset in b).

are similar for the three samples, which correspond to the tail for the PL spectra in Fig. 9.

In the TRPL spectra, a rapid decrease in intensity after excitation is typically explained in terms of fast electronic relaxation processes. Right after the 100 fs pulse, this rapid decrease, particularly for the AP-CNDs, could be explained in terms of mainly fast non-radiative recombination of excited carriers occurring, which must be highly promoted through defects, surface traps, or highly efficient energy loss mechanisms, before slower radiative recombination becomes dominant.[94] It has been established that fast intensity decay in TRPL is mostly due to non-radiative recombination channels dominating early times.[95] Also, if there are many defects, surface traps (functional groups, for example), or high carrier densities, electrons and holes quickly lose their energy without emitting light.[94,96]

It can also be noted that immediately after the excitation pulse, a high density of excited carriers is allowed, which means many non-radiative centers, defects, impurities, or surface states, as mentioned above, are available to capture these carriers very efficiently.[97] As these traps fill or as carriers recombine, the available pathways decrease, and the rate of decay slows down, which can explain the observed decay in the inset of Fig. 12b.

Finally, TRPL measurements were used to approximate the lifetimes of the CNDs by fitting the decay curves in Fig. 12 with a single exponential function ($1/e$), determining the lifetimes when the intensity is around 36% of the intensity for each sample.[98] For the OP-CNDs (blue lines), recorded at emission wavelengths of 410 nm, 435 nm, and 540 nm under 350 nm excitation, the decay was best described by a single-component model,[99,100] yielding lifetimes of 1.53 ns, 1.75 ns, and 2.21 ns, respectively. In the case of the AP-CNDs (orange lines), the same approach gave shorter lifetimes of 0.27 ns, 0.21 ns, and 1.26 ns at the corresponding emission wavelengths. For the SCG-CNDs (purple lines), the fitted single-component decay resulted in lifetimes of 1.15 ns, 1.58 ns, and 1.91 ns, respectively. The PL of pure pCNDs, synthesized under mild and controlled conditions, was reported and described by a three-component decay with lifetimes of 1.9, 5.4, and 8.8 ns, being the second very large compared with the lifetimes reported here.

The differences in lifetimes can be directly correlated with the functionalized groups detected on the surface of the nanodots (as shown from IR and XPS analysis), which strongly influence their electronic structure and surface chemistry. As mentioned above, in CNDs, photoluminescence is predominantly associated with surface functional groups and defect states rather than quantum confinement, as is typical in carbon quantum dots. The presence of C=C bonds, containing sp^2-hybridized carbon, provides conjugated π-electron systems that can absorb in the UV region and contribute to intrinsic fluorescence through $\pi \rightarrow \pi^*$ transitions. These conjugated domains act like molecular fluorophores, where excited π electrons undergo radiative recombination. In contrast, oxygen-containing groups such as –OH and C–O, commonly found at the surface, introduce trap states that favor non-radiative recombination pathways, leading to reduced lifetimes. The shorter lifetimes of the AP-CNDs, therefore, suggest a higher density of surface defects or oxygen-rich groups, consistent with their more intense but less stable PL emission. In comparison, the longer lifetimes observed for OP-CNDs and SCG-CNDs could indicate a stronger contribution from intrinsic sp^2 domains and fewer non-radiative channels.

Conclusions

This study establishes picosecond laser ablation of waste-derived biocarbon in water as a fast, single-step, and reagent-free route to functional water-soluble carbon nanodots. By juxtaposing three commonplace agri-food wastes, we demonstrate that precursor chemistry dictates nanodot architecture. Lignin-rich, amorphous avocado biocarbon yields ultra-small (<3 nm), defect-rich dots with intense blue-green photoluminescence. In contrast, more ordered orange- and coffee-derived carbons preferentially form larger, graphitic nanoparticles with diminished emission. Surface-retained

oxygenated groups, not quantum confinement, underpin the excitation-dependent PL. FTIR, multi-peak PL fitting, and XPS analysis show that carboxyl, hydroxyl, and carbonyl moieties inherited from the parent biomass act as radiative trap states.

Laser fragmentation affords a green advantage. Ten-minute processing in pure water surpasses hours-long hydrothermal or chemically assisted protocols, negates acid/alkali waste streams, and preserves water solubility without post-passivation. Waste valorization meets high-value functionality. Converting everyday peels and spent ground into stable, brightly emissive nanodots aligns with circular economy goals while furnishing ready-to-use probes for bio-imaging, environmental sensing, and low-toxicity photonics. Collectively, these findings advance the field by coupling feedstock-to-function design rules with an ultrafast, eco-compatible fabrication strategy. The methodology can be extended to other biomass residues and laser parameters, paving the way to produce tailored carbon nanodots, with progressive scalability and reinforcing the role of photonic processing in sustainable nanochemistry.

Conflicts of interest

There are no conflicts to declare.

Data availability

The data are available in the SI Section. Supplementary information is available. See DOI: **https://doi.org/10.1039/d5na00560d**.

Acknowledgements

DRC Thanks to the Talented Young Scientific Program from the Chinese government for the support to perform experimental research at IFFS-UESTC. We acknowledge BSc Lázaro Huerta Arcos for the XPS measurements at the XPS Lab from the Instituto de Investigaciones en Materiales, UNAM, and funding from PAPIIT - UNAM IG100825.

References

1 R. Vithalani, D. Patel, C. K. Modi and D. H. Suthar, *J. Mater. Sci.*, 2020, **55**, 8769.
2 B. N. Kumara, P. Kalimuthu and K. S. Prasad, *Anal. Chim. Acta*, 2023, **1268**, 341430.
3 R. Lamba, Y. Yukta, J. Mondal, R. Kumar, B. Pani and B. Singh, *ACS Appl. Bio Mater.*, 2024, **7**, 2086.
4 S. K. Debnath and R. Srivastava, *Front. nanotechnol.*, 2021, **3**, 644564.
5 H. Ding, T. Xiao, F. Ren, Y. Qiu, Z. Shen, X. Chen, E. Mijowska and H. Chen, *BMEMat*, 2024, e12085.
6 H. L. Yang, L. F. Bai, Z. R. Geng, H. Chen, L. T. Xu, Y. C. Xie, D. J. Wang, H. W. Gu and X. M. Wang, *Mater. Today Adv.*, 2023, **18**, 100376.
7 X. Guan, Z. Li, X. Geng, Z. Lei, A. Karakoti, T. Wu and A. Vinu, *Small*, 2023, **19**, 2207181.
8 K. S. Das, Y. Liu, S. Yeom, D. Y. Kimand and C. L. Richards, *Nano Lett.*, 2014, **14**, 620.
9 Y. Kwee, A. N. Kristanti, K. Siimon, N. S. Aminah and M. Z. Fahmi, *S. Afr. J. Chem.*, 2021, **75**, 40.
10 K. W. Kim, Y. M. Kwon, S. Y. Kim and J. Y. H Kim, *Electron. J. Biotechnol.*, 2022, **56**, 22.
11 D. Reyes, M. Camacho, M. A. Camacho, M. Mayorga, D. Weathers, G. Salamo, Z. Wang and A. Neogi, *Nanoscale Res. Lett.*, 2016, **11**, 424.
12 L. Torrisi, A. Torrisi and L. Cutroneo, *Fullerenes, Nanotub. Carbon Nanostruct.*, 2025, **33**, 111.
13 A. Kaczmarek, A. Wisniewska, T. Mościcki and J. Hoffman, *Materials*, 2024, **17**, 1573.
14 G. K. YogeshK, S. Shukla, D. Sastikumar and P. Koinkar, *Appl. Phys. A*, 2021, **127**, 1.
15 M. Ghasemlou, N. Pn, K. Alexander, A. Zavabeti, P. C. Sherrell, E. P. Ivanova, B. Adhikari, M. Naebe and S. K. Bhargava, *Adv. Mater.*, 2024, **36**, 2312474.
16 H. Liu, X. Zhong, Q. Pan, Y. Zhang, W. Deng, G. Zou, H. Hou and X. Ji, *Coord. Chem. Rev.*, 2024, **498**, 215468.
17 F. R. U. Cortes, E. Falomir, J. Lancis and G. Mínguez, *Appl. Surf. Sci.*, 2024, **665**, 160326.
18 D. Reyes, M. Camacho, L. Buendía, M. A. Camacho, B. Squires and A. Neogi, *Int. J. Opt. Photonic Eng.*, 2022, **7**, 047.
19 P. Kaur and G. Verma, *Mater. Today Sustain.*, 2022, **18**, 100137.
20 H. Ashraf and B. D. Karahan, *Mater. Res. Bull.*, 2024, **169**, 112492.
21 S. Sharma, R. Kumar, K. Kumar and N. Thakur, *Mater. Sci. Eng., B*, 2024, **305**, 117414.
22 N. Oladzadabbasabadi, M. A. Dheyab, A. M. Nafchi, M. Ghasemlou, E. P. Ivanova and B. Adhikari, *Adv. Colloid Interface Sci.*, 2323, **321**, 103020.
23 D. Gupta, R. Priyadarshi, S. K. Tammina, J. W. Rhim and G. Agrawal, *Food Bioprocess Technol.*, 2024, **1**, 1–25.
24 H. Zhang, S. Wu, Z. Xing and H. B. Wang, *Analyst*, 2021, **146**, 7250.
25 S. Y. Park, H. U. Lee, E. S. Park, S. C. Lee, J. W. Lee, S. W. Jeong, C. H. Kim, L. C. Lee, Y. S. Hu and J. Lee, *ACS Appl. Mater. Interfaces*, 2014, **6**, 3365.
26 M. Medhi, M. Yumnam, P. Mudoi and P. Mishra, *J. Lumin.*, 2025, **277**, 120926.
27 F. Anindita, L. Naani, D. Permana, K. Karelius and Y. I. Kedang, *Journal of The Indonesian Society of Integrated Chemistry*, 2024, **16**, 140.
28 A. J. G. Afonso, F. T. Aquino, G. M. Dalmonico, M. V. Nascimento, E. Wrasse and K. M. R. de Aguiar, *Carbon Lett.*, 2022, **32**, 131.
29 S. Chahal, J. R. Macairan, N. Yousefi, N. Tufenkji and R. Naccache, *RSC Adv.*, 2021, **11**, 25354.
30 D. S. Chauhan, M. A. Quraishi and C. Verma, *Carbon Lett.*, 2022, **32**, 1603.
31 J. Li, L. Zhang, P. Li, Y. Zhang and C. Dong, *Sensors and Actuators B*, 2018, **258**, 580.
32 N. K. Quang, N. N. Hieu, V. V. Q. Bao, V. T. Phuoc, L. Q. Doc, N. M. Tri and C. T. C. Ha, *N. Carbon Mater.*, 2022, **375**, 95.

33 V. Bressi, C. Celesti, A. Ferlazzo, T. Len, K. Moulaee, G. Neri, R. Luque and C. Espro, *Nano*, 2024, **11**, 1245.
34 N. A. Nazibudin, M. F. Zainuddin and C. A. C Abdullah, *J. Adv. Res. Fluid Mech. Therm. Sci.*, 2023, **101**, 192.
35 V. Bressi, A. M. Balu, D. Iannazzo and C. Espro, *Curr. Opin. Green Sustainable Chem.*, 2023, **40**, 100742.
36 S. Sawalha, M. Assali, A. Nasasrah, M. Salman, M. Nasasrah, M. Jitan, H. S. Hilal and A. Zyuod, *RSC Adv.*, 2022, **12**, 4490.
37 X. W. Tan, A. N. B. Romainor, S. F. Chin and S. M. Ng, *J. Anal. Appl. Pyrolysis*, 2014, **105**, 157.
38 K. Y. Aung, Q. Li, M. Wei, F. Chen and T. Yan, *J. Anal. Appl. Pyrolysis*, 2024, **183**, 106724.
39 U. M. Lad, N. P. Chunekar, D. J. Dave, B. N. Desai, D. H. Suthar and C. K. Modi, *J. Fluoresc.*, 2024, **34**, 2895.
40 M. Ahmad, M. A. Akanji, A. R. Usman, A. S. Al-Farraj, Y. F. Tsang and M. I. Al-Wabel, *Sci. Rep.*, 2020, **10**, 16125.
41 X. Zhang, K. Zhang, X. Yao, Z. Wu, C. Lv and Q. Li, *Int. J. Environ. Anal. Chem.*, 2020, **102**, 4768.
42 N. Enríquez, A. R. Vilchis, S. Camacho, M. A. Camacho and M. Camacho, *Superficies Vacio*, 2024, **37**, 240901.
43 B. Zapata, J. Balmaseda, E. Fregoso and E. Torres, *J. Therm. Anal. Calorim.*, 2009, **98**, 309.
44 Z. Qin, H. M. Liu, X. C. Cheng and X. D. Wang, *Int. J. Biol. Macromol.*, 2019, **137**, 801.
45 A. Del Castillo, B. Rodríguez, P. G. Del Río, G. Eibes, G. Garrote and B. Gullón, *Bioresour. Technol.*, 2021, **342**, 125981.
46 B. Gullón, G. Eibes, I. Dávila, M. T. Moreira, J. Labidi and P. Gullón, *Carbohydr. Polym.*, 2018, **192**, 75.
47 T. S. Andrade, J. Vakros, D. Mantzavinos and P. Lianos, *Chem. Eng. J. Adv.*, 2020, **4**, 100061.
48 M. Jeguirim, L. Limousy and P. Dutournie, *Chem. Eng. Res. Des.*, 2014, **92**, 1876.
49 Y. M. Faleeva, V. A. Lavrenov and V. M. Zaichenko, *Biomass Conv. Bioref.*, 2024, **14**, 14519.
50 B. Du, H. Zhu, X. Wang, L. P. Xiao, J. Ma, X. Chen and R. C. Sun, *Int. J. Biol. Macromol.*, 2021, **174**, 254.
51 L. T. Tran, M. Q. Nguyen, H. T. Hoang, H. T. Nguyen and T. H. T Vu, *J. Chem.*, 2022, **1**, 1.
52 C. Guizani, K. Haddad, L. Limousy and M. Jeguirim, *Carbon*, 2017, **119**, 519.
53 M. W. Smith, B. Pecha, G. Helms, L. Scudiero and M. Garcia, *Biomass Bioenergy*, 2017, **104**, 17.
54 Y. Lee, K. Yang, N. D. Anh, C. Park, S. M. Lee and T. G. Lee, *Appl. Surf. Sci.*, 2021, **536**, 147990.
55 J. Martinez, D. Reyes, E. Vigueras, C. Patino, J. A. Reyes, V. H. Castrejon and I. Garcia, *Carbon Lett.*, 2022, **32**, 475.
56 J. Xu, J. Liu, P. Ling, X. Zhang, K. Xu, L. He and J. Xiang, *Energy*, 2020, **202**, 117644.
57 D. V. D. Sousa, L. M. Guimarães, J. F. Felix and J. C. Ker, *PloS One*, 2020, **15**, e0229447.
58 A. Sadezky, H. Muckenhuber, H. Grothe and R. Niessner, *Carbon*, 2005, **43**, 1731.
59 J. Yu, L. Sun, C. Berrueco, B. Fidalgo, N. Paterson and M. Millan, *J. Anal. Appl. Pyrolysis*, 2018, **130**, 127.
60 J. Marquina, C. Power and J. González, *Tumbaga*, 2010, **1**, 183.
61 H. Ming, Z. Ma, Y. Liu, K. Pan, H. Yu, F. Wang and Z. Kang, *Dalton Trans.*, 2012, **41**, 9526.
62 X. T. Tian and X. B. Yin, *Small*, 2019, **15**, 1901803.
63 D. W. Boukhvalov, V. Y. Osipov, D. Murzalinov, A. Serikkanov and H. A. Bi, *Carbon*, 2024, **225**, 119101.
64 J. T. Margraf, V. Strauss, D. M. Guldi and T. Clark, *J. Phys. Chem. B*, 2015, **119**, 7258.
65 L. Wang, L. Yu, H. Ge, Y. Bu, M. Sun, D. Huang and S. Wang, *Microchem. J.*, 2022, **175**, 107181.
66 C. Chen, Z. Xu, J. Qiu, W. Ye, X. Xu, R. Wang, C. Hu, J. Zhuang, B. Lei, W. Li, X. Zhang, G. Hu and Y. Liu, *ACS Appl. Nano Mater.*, 2022, **5**, 9140.
67 X. Huang, W. Ye, J. Zhuang, C. Hu, H. Dong, B. Lei and Y. Liu, *ACS Sustain. Chem. Eng.*, 2024, **12**, 10399.
68 Y. Xu, D. Li, M. Liu, F. Niu, J. Liu and E. Wang, *Sci. Rep.*, 2017, **7**, 4499.
69 K. Anpalagan, H. Yin, I. Cole, T. Zhang and D. T. H. Lai, *Inorganics*, 2024, **12**, 96.
70 O. Dimitriev, D. K. A. Zaderko, O. Isaieva, A. Vasin, Y. Piryatinski, M. Fahlman and A. Nazarov, *Nanoscale Adv.*, 2024, **6**, 2185.
71 M. A. Issa, Z. Z. Abidin, M. Y. Pudza and H. Zentou, *RSC Adv.*, 2020, **10**, 14979.
72 H. Wang, L. Han, Y. Gao, X. Gao, W. He, C. Shan, W. Fan, Y. Guo, M. Gao and H. Cheng, *J. Fluoresc.*, 2025, 1–11.
73 L. Qin, Y. Song, Y. Zhang, W. Gao, X. Meng, Y. Bai, K. Geng, P. Niu, Y. Wang, N. Wu, J. Bai, J. Ma and L. Ren, *J. Colloid Interface Sci.*, 2025, **679**, 135.
74 D. M. Arvapalli, A. T. Sheardy, K. C. Alapati and J. Wei, *Talanta*, 2020, **209**, 120538.
75 B. Salehi, B. Zhang, K. Nowlin, L. Wang and A. Shahbazi, *Carbohydr. Polym.*, 2024, **327**, 121657.
76 B. Kumar, Ø. Sele and A. H. Tadaaki, *ACS Sustain. Chem. Eng.*, 2021, **9**, 9879.
77 W. J. Liu, W. W. Li, H. Jiang and H. Q. Yu, *Chem. Rev.*, 2017, **117**, 6367–6398.
78 A. L. Sullivan and R. Ball, *Atmos. Environ.*, 2012, **47**, 133.
79 J. Kibet, L. Khachatryan and B. Dellinger, *Environ. Sci. Technol.*, 2012, **46**, 12994.
80 M. A. Czarnecki, Y. Morisawa, Y. Futami and Y. Ozaki, *Chem. Rev.*, 2015, **115**, 9707.
81 A. Mtibe, M. J. John, J. E. Andrew and T. C. Mokhena, *Biomaterials and Polymers Horizon*, 2022, **1**, 1.
82 A. K. Mohanty, S. Vivekanandhan, O. Das, L. M. Romero Millán, N. B. Klinghoffer, A. Nzihou and M. Misra, *Nat. Rev. Methods Primers*, 2024, **4**, 19.
83 W. Shen, Z. Li and Y. Liu, *Recent Pat. Chem. Eng.*, 2008, **1**, 27.
84 C. Xu, X. Shi, A. Ji, L. Shi, C. Zhou and Y. Cui, *PLoS One*, 2015, **10**, e0144842.
85 K. J. Mintz, M. Bartoli, M. Rovere, Y. Zhou, S. D. Hettiarachchi, S. Paudyal, J. Chen, J. B. Domena, P. Y. Liyanage, R. Sampson, D. Khadka, R. R. Pandey, S. Huang, C. C. Chusuei, A. Tagliaferro and R. M. Leblanc, *Carbon*, 2021, **173**, 433.
86 A. A. Manshina, I. I. Tumkin, E. M. Khairullina, M. Mizoshiri, A. Ostendorf, S. A. Kulinich, S. Makarov,

A. A. Kuchmizhak and E. L. Gurevich, *Adv. Funct. Mater.*, 2024, **34**, 2405457.
87 P. P. Debes, M. Langer, M. Pagel, E. Menna, B. Smarsly, S. Osella, J. Gallego and T. Gatti, *ChemNanoMat*, 2024, **10**, e202300471.
88 C. Zhang and J. Lin, *Chem. Soc. Rev.*, 2012, **41**, 7938.
89 Y. Xu, D. Li, M. Liu, F. Niu, J. Liu and E. Wang, *Sci. Rep.*, 2017, **7**, 4499.
90 Q. Chen, L. Chen, X. Nie, H. Man, Z. Guo, X. Wang, J. Tu, G. Jin and L. Ci, *Ecotoxicol. Environ. Saf.*, 2020, **206**, 111220.
91 M. W Barsoum, A. Crossley and S. Myhra, *J. Phys. Chem. Solids*, 2002, **63**, 2063.
92 F. Arcudi, L. Dordevic and M. Prato, *Angew. Chem., Int. Ed.*, 2016, **55**, 2107.
93 J. A. Gardella, S. A. Ferguson and R. L. Chin, *Appl. Spectrosc.*, 1986, **40**, 224–232.
94 L. Li and T. Dong, *J. Mater. Chem. C*, 2018, **6**, 7944.
95 M. C. Ortega, N. X. Chung, R. Limpens, L. Gomez, J. L. Hueso, J. Santamaria and T. Gregorkiewicz, *Carbon*, 2017, **117**, 437.
96 J. Li, X. Zhao and X. Gong, *Smaill*, 2024, **20**, 2400107.
97 K. Muthamma, D. Sunil and P. Shetty, *Appl. Mater. Today*, 2021, **23**, 101050.
98 J. E. Martin and L. E. Shea-Rohwer, *J. Lumin.*, 2006, **121**, 573.
99 S. Y. Song, K. K. Liu, Q. Cao, X. Mao, W. B. Zhao, Y. Wang, Y. C. Liang, J. H. Zang, Q. Lou, L. Dong and C. X. Shan, *Light: Sci. Appl.*, 2022, **11**, 146.
100 V. Strauss, J. T. Margraf, C. Dolle, B. Butz, T. J. Nacken, J. Walter, W. Bauer, W. Peukert, E. Spiecker, T. Clark and D. M. Guldi, *J. Am. Chem. Soc.*, 2014, **136**, 17308.